

Non-contact assessment of pneumonia in low and middle income countries



Dineo Serame

Hertford College

Supervised by

Professor Lionel Tarassenko, Dr. Mauricio Villarroel

Department of Engineering Science

University of Oxford

Abstract

Pneumonia is an illness usually caused by an acute respiratory tract infection in which lungs become inflamed and congested, limiting oxygen intake and leading to breathlessness. Despite the reduction in cases among children under the age of 5, pneumonia is still the main cause of childhood death in low income countries in Asia and Africa. The global community has therefore committed to ending preventable mortality and morbidity caused by pneumonia by 2025. To achieve this goal, the World Health Organisation (WHO) developed a pneumonia control strategy which provides clinical case management guidelines to offer a basic standard for appropriate assessment and treatment of sick children in Low and Middle Class-Income Countries (LMIC). However, due to factors such as inadequate training and supervision, as well as a shortage of skilled health professionals, adherence to these strategies remain poor in many settings. This failure in guideline implementation is further compounded by large numbers of seriously ill children in need of care.

The WHO recommends the use of raised respiratory rate (RR) and chest wall in-drawing to help health workers in developing countries to diagnose pneumonia. A particular problem, however, is the accuracy and reliability of identification of these key clinical features of pneumonia by junior clinicians. Guidelines on diagnosis, hospital admission and ultimately treatment require clinicians to measure respiratory rate by counting chest wall movements and assess the degree of respiratory distress by physical examination. Studies have shown poor inter-observer agreement for assessing clinical signs, thus technologies that can accurately identify and standardise assessment of respiratory distress would be a major advance towards improving the efficiency and quality of clinical assessment and, ultimately, clinical outcomes for pneumonia.

Smartphones offer a platform for developing these technologies to help healthcare professionals consistently identify clinical signs of severe illness, improve diagnosis of pneumonia and assess its severity. Smart phone cameras have the potential to enable standardised recognition of clinical signs of respiratory distress based on image processing and machine learning algorithms. These advances, combined with low-cost sensors (e.g. for oxygen saturation or temperature measurement), could result in a new generation of decision support tools. The same technology may also contribute towards refining existing WHO clinical algorithms amid growing concerns of diminished specificity of current guidelines for reliably identifying bacterial pneumonia in the post-pneumococcal and Haemophilus I vaccine era.

This transfer report covers the development of algorithms for estimation of heart rate (HR) and RR across two clinical datasets. In chapter 3, red and near-infrared signals from a wrist-worn photoplethysmography (PPG) device were used to estimate HR ($r = 0.99$, MAE 1.2 = beats/minute) and RR ($r = 0.67$, MAE = 1.6 breaths/minute) during periods of induced hypoxia in a clinical study involving healthy volunteers. In chapter 4, video data from an observational neonatal intensive care unit (NICU) study was used to estimate HR ($r = 0.83$, MAE = 3.2) and RR ($r = 0.71$, MAE = 5.3). These results show that the algorithms developed are applicable in realistic scenarios using data from both wearables and video cameras.

Table of contents

Table of contents	v
List of figures	vii
List of tables	viii
List of abbreviations	ix
1 Introduction	1
1.1 Motivation	1
1.2 Pneumonia	1
1.2.1 Symptoms and causes.....	1
1.2.2 Diagnosis.....	2
1.2.3 Treatment.....	2
1.3 Challenges in LMIC	3
1.4 Objectives	4
1.5 Contributions	4
1.6 Outline of the report	4
2 Literature review	5
2.1 Introduction	5
2.2 Diagnostic Innovations	6
2.2.1 Pulse oximetry	6
2.2.2 Lung auscultation.....	6
2.2.3 Other innovations	6
2.3 Vital sign acquisition and estimation	6
2.3.1 Pulse oximetry	7
2.3.2 Wearable technology.....	7
2.3.3 PPG imaging	8
2.4 Respiratory signal processing	9
2.4.1 Respiratory signal extraction	9
2.4.2 Signal processing techniques	10
3 Vital sign estimation using wearable devices	11
3.1 Introduction	11
3.2 Data set	11
3.2.1 Participant recruitment and assessment	11
3.2.2 Study set-up	11
3.2.3 Instrumentation	12
3.2.4 Data selection	12
3.3 Heart rate estimation	14
3.3.1 Overview of the process	14
3.3.2 Filtering	14
3.3.3 Peak detection.....	14
3.3.4 Motion SQI.....	15
3.3.5 Heart rate computation	16
3.3.6 Time alignment between heart rate from Philips and HR estimated from the Wavelet Health device	16
3.4 Respiratory rate estimation.....	17
3.4.1 Overview of the process	17
3.4.2 Extracting respiratory signal	18
3.4.3 RR estimation	20
3.5 Oxygen saturation	20

3.5.1	Overview of the process	20
3.5.2	Filtering	20
3.5.3	Signal amplitude.....	20
3.5.4	Computing Red/NIR Ratios.....	21
3.6	Results	21
3.6.1	Error metrics.....	21
3.6.2	Heart rate	22
3.6.3	Respiratory rate	23
3.6.4	SpO_2	24
3.7	Discussion	26
3.8	Conclusion	26
	Bibliography	27

List of figures

2.1	Global causes of childhood deaths.	5
2.2	A typical PPG waveform.....	8
2.3	Modulation of the PPG signal due to respiration.	9
3.1	Reference physiological parameters recorded by the Phillips monitor and the Wavelet Health device.	13
3.2	Flow diagram outlining the patient selection process.	13
3.3	Distribution of vital signs recorded by the Philips monitor for the 10 sessions selected for analysis.....	13
3.4	Flow diagram outlining the process of computing heart rate from the NIR signal from the Wavelet Health device.....	14
3.5	Magnitude responses.	14
3.6	60-second sample time series from the NIR waveform.....	15
3.7	Detection of peaks and troughs on the NIR signal over a 15-second sample window.	16
3.8	Using motion SQI to discard time periods corresponding to motion artefacts.	16
3.9	Flow diagram outlining the process of computing respiratory rate from the NIR signal recorded by the Wavelet Health wearable device.	17
3.10	60-second example of the amplitude modulation method being used to estimate RR from the NIR signal.	18
3.11	Filter magnitude responses.	19
3.12	60-second example of the frequency modulation method used to estimate RR from the NIR signal.	19
3.13	Flow diagram outlining the process of computing the relationship between the ratio of ratios of the red and NIR signals recorded by the Wavelet Health device and the reference SpO_2 from the Philips monitor.	20
3.14	Magnitude responses.	21
3.15	Comparison between HR provided by the Philips monitor and the HR estimates computed by the proposed algorithms.	22
3.16	Comparison between the reference and estimated heart rate for the 10 patients analysed..	23
3.17	Comparison between the reference respiratory rate provided by the Philips monitor and the estimated respiratory rates.	23
3.18	Comparison between the reference and estimated RR for the 10 patients in the dataset. ...	24
3.19	Comparison of the trend between the Red/NIR ratio and the reference SpO_2	25
3.20	Correlation plots of the Red/NIR Ratio for the 10 patients in the dataset.	25

List of tables

2.1	Summary of diagnostic innovations that have been recently developed, or are currently under development in the context of childhood pneumonia.	7
3.1	Summary of the population in the clinical study.	12
3.2	Summary of results for the proposed algorithms to estimate HR from the NIR signals for the 10 patients analysed.	22
3.3	Summary of the results for the proposed algorithms to estimate respiratory rate.	24

List of abbreviations

SpO_2 Peripheral oxygen saturation, as measured by a pulse oximeter.

CHW Community Health Worker.

DC non-pulsatile component of the plethysmograph signal.

HR Heart rate.

LMIC Low and Middle Income Countries.

MAD Mean Absolute Deviation.

MAE Mean Absolute Error.

PPG Photoplethysmography.

RMSE Root Mean Square Error.

ROI Regions of Interest.

RR Respiratory rate.

SQI Signal Quality Index.

Chapter 1

Introduction

1.1 Motivation

Despite a general improvement in living conditions, improved nutrition, introduction of vaccines and greater access to healthcare, pneumonia remains the biggest cause of mortality in children under the age of 5, accounting for more than 15% of childhood deaths globally [55]. In 2011, there were an estimated 120 million episodes of childhood pneumonia globally, of which 14 million advanced to severe disease, leading to 1.3 million deceased cases. Most deaths (81%) occurred in children under 2 years of age. The highest incidences of severe cases were in Southeast Asia (39%) and Africa (30%) [62]. Hospitalisation of children with pneumonia in Low and Middle Income Countries (LMIC) increased from 7% to 50% between 2000 and 2015 [32].

Shortage of clinical expertise, high-quality treatment facilities and availability of adequate medical equipment in LMIC prevents early detection and treatment of pneumonia in children. Timely and accurate diagnosis that facilitates appropriate treatment could reduce mortality by as much as 42% [61]. While high-income countries remain at the forefront of developing the latest mobile technologies used in healthcare, the rate of penetration of such technologies in LMICs has recently exceeded that of their wealthier neighbours [6]. My research therefore aims to develop and implement low-cost, user friendly smart phone algorithms to assist the existing clinical staff in the diagnosis of childhood pneumonia in LMIC areas.

1.2 Pneumonia

Pneumonia is a highly prevalent acute respiratory infection. The disease is caused by pathogens such as bacteria, viruses or fungi causing an inflammation in the lungs. The alveoli (the microscopic air sacks in the lungs where oxygen and carbon dioxide exchange occurs) get filled up with fluid and pus, decreasing lung compliance (the change in volume per unit change in pressure). This leads to reduced volume for gas exchange and difficulty in breathing, affecting oxygen supply to the bloodstream [2].

1.2.1 Symptoms and causes

Children diagnosed with pneumonia often present symptoms of fast breathing, classified by the World Health Organisation (WHO) as having a respiratory rate (RR) ≥ 50 breaths/min in a child aged 2-11 months and ≥ 40 breaths/min in a child aged 1-5 years [41]. In most cases, illness begins as an upper respiratory tract infection and progresses gradually over several days, with increasing severity of cough and respiratory distress. To maintain an adequate supply of air in the lungs during the respiratory cycle with the decreased lung compliance caused by pneumonia, greater inspiratory force is needed. Consequently, the subcostal tissue on the chest is pulled inward during inspiration, producing what the WHO Integrated Management of Childhood Illness (IMCI) guidelines define as chest in-drawing [33]. Children with a cough, difficulty

breathing and chest in-drawing are considered to have severe pneumonia. Very severe pneumonia can be detected from the presence of central cyanosis (blue colour tint in skin, hips or mucus membranes), a peripheral oxygen saturation (SpO_2) < 90%, severe respiratory distress or the inability to breastfeed [3].

In severely ill infants and toddlers with a rapid onset and progression of symptoms of pneumonia, the bacteria *Streptococcus pneumoniae* is often the predominant cause of infection. It is estimated to cause 18% of severe cases and 33% of deaths. In 2016, *Streptococcus pneumoniae* was the leading cause of lower respiratory infection morbidity and mortality globally, contributing to more deaths than all other aetiologies combined [56]. Other important pathogens include *Haemophilus influenzae type b* (*Hib*), estimated to account for 4% of severe episodes and 16% of deaths; and *influenza virus*, which is associated with approximately 7% of severe episodes and 11% of deaths. Stagno *et al* [48] found that the presence of more than one pathogen was significantly associated with more frequent requirements for oxygen and mechanical ventilation. These pathogens can infect a child either through air droplets (e.g. from a cough) or through contaminated blood (especially during and shortly after birth) and contribute to the progression of illness.

1.2.2 Diagnosis

Even though there are guidelines on recognising pneumonia, diagnosis can often be challenging because the clinical manifestation of pneumonia in children is variable [47]. X-rays, in combination with arterial blood gas tests (ABGs), auscultation of the lungs using a stethoscope, heart rate, SpO_2 , temperature and respiratory rate count are typically used as diagnostic mechanisms [12]. Signs of chronic airflow obstruction, hyperinflation and various abnormalities of chest wall motion are also used to diagnose pneumonia. The WHO recommends that community health workers treat pneumonia in children according to specific case-management algorithms and use respiratory rate (RR) and chest in-drawing for diagnosis [42].

The measurement of other vital signs such as SpO_2 , heart rate (HR) and temperature allows clinicians to have a more complete view of the child's physiology. These vital signs help guide the hospital admission decisions for pneumonia as well as the treatment of other accompanying diseases or complications [31]. RR, HR, and SpO_2 are monitored in those with severe pneumonia or requiring regular oxygen therapy. The gold standard for assessing oxygen saturation is arterial blood gas measurement. However, it is time consuming and invasive. Pulse oximetry is therefore commonly used in hospital settings to monitor pneumonia patients and has also been recommended for use in the community [24].

The most common methods to measure RR and HR are counting breaths using observation and auscultation of the heart respectively. However, it can be difficult to identify breaths and maintain a count when estimating RR by manually counting breaths. Clinically, RR is computed using electrodes attached to the patient's chest, a technique called impedance pneumography (IP) [5]. This technique often requires expensive devices and therefore is not commonly used in LMICs. HR auscultation has similar challenges to counting breaths.

1.2.3 Treatment

IMCI guidelines indicate when referral for pneumonia treatment is needed and specify the appropriate antimicrobial agents when referral is not needed. The guidelines state that treatment should target the bacterial causes most likely to lead to severe disease, including *streptococcus pneumoniae* and *Haemophilus influenzae*. Identification of the causative pathogen of pneumonia is however challenging as few children

develop bacteraemic illness, where bacteria is present in the blood stream and detected through blood cultures [62]. Furthermore, only a third of pneumonia cases can be attributed to a certain aetiology via culture, antigen detection or clinically available serological techniques [34]. Most diagnostic tests for pneumonia pathogens have suboptimal diagnostic sensitivity. Blood cultures are frequently performed for hospitalised pneumonia patients but are positive only in <10% of cases [36].

A 2005 technical update of the WHO IMCI guidelines recommended the administration of amoxicillin (50 mg/kg per dose, in two divided doses), with co-trimoxazole as an alternative in the treatment of non-severe pneumonia in some settings. Treatment failure was defined in a child who develops pneumonia signs warranting immediate referral or who did not have a decrease in respiratory rate after 48 – 72 hours of therapy [22]. Suitable recommended treatments include the administration of a high-dose antibiotic (i.e. amoxicillin-clavulanic acid) for children over 3 years of age.

Between 2010 and 2013, more than 54 countries supported by the Global Alliance for Vaccines and Immunisation (GAVI) issued recommendations for paediatric pneumonia treatment, implementing the pneumococcal conjugate vaccine protocols[45]. These recommendations were primarily intended for high to middle-income nations. However, new information on antimicrobial resistance, the changing epidemiology of pneumonia and the availability of a broader range of antimicrobial agents prompted the need to update the guidelines. With improved vaccine uptake, the prevalence of vaccine-targeted pathogens may diminish, while a greater proportion of cases may occur due to *Staphylococcus aureus*, *Klebsiella pneumoniae* and *Mycobacterium tuberculosis* in tuberculosis (TB) endemic areas such as Sub-Saharan Africa. [62]. New guidelines are needed for antimicrobial treatment of non-severe pneumonia among children assessed by first-level health providers, often with basic health training.

1.3 Challenges in LMIC

Strategies for prevention, diagnosis and treatment of pneumonia are well documented and are mostly effective in resource-rich settings. However, the accuracy and viability of most diagnostic tools for pneumonia have not been assessed or validated in LMIC. The reference standard for the diagnosis of pneumonia is the extraction of fluid or tissue samples from the lower respiratory tract. Such invasive measures are reserved for patients with severe or life-threatening pneumonia who do not respond to first-line therapies. In general practice, a chest radiograph is considered a clinical reference standard for pneumonia given it is well studied in the literature, is readily available in low-resource settings and is less invasive.

Because of limited resources in LMIC, timely diagnosis of pneumonia is a challenge. The WHO recommendations rely on simple clinical signs: tachypnoea or respiratory distress in a child with cough or difficulty breathing. Community health workers are trained to count the respiratory rate of a child with cough and/or difficulty breathing. The health workers determine whether the child has fast breathing or not based on how the child's respiratory rate relates to generic cut-off thresholds. Counting the number of breaths is typically performed manually with the aid of watches or timers [16], [40]. However, even with these counting aids, measuring a child's respiratory rate through visual observation requires focused concentration and can be challenging in a child who may be moving, crying or breathing rapidly. Inaccurate or imprecise measurements can stem from factors including poor visibility of the start or end of a breath, an irritable or moving child, or difficulty counting or remembering the count [19]. Until now, there has been limited evidence on the efficacy of technology and other affordable tools to help community health workers in resource-poor settings improve the classification of fast breathing or other breathing patterns for the

diagnosis of pneumonia.

The uncertainty surrounding the diagnosis of pneumonia has therefore contributed to antibiotic overuse in children with viral respiratory tract infections. Thus, there is an urgent need to rethink existing practises of using manual breath counts for RR estimation as a stand-alone criteria for diagnosing pneumonia. Cost effective, portable, non-contact methods can be useful in diagnosing pneumonia, particularly in LMIC. If diagnosed early, targeted antibiotic therapy can be initiated to effectively treat the disease.

Recent advances have shown that estimation of vital signs such as HR and RR through non-contact means is viable. This estimation can even be achieved using typical smart phone cameras. Such an approach would allow for the accurate estimation of these vital signs without requiring expensive specialised equipment and clinical expertise. These vital signs estimates, if made available in LMIC, may aid in the early detection and diagnosis of childhood pneumonia.

1.4 Objectives

The main aim of my DPhil is to develop non-contact video based algorithms to identify breathing patterns and signs of respiratory distress in children diagnosed with pneumonia in LMIC using the video cameras available in smartphones. The algorithms will be implemented as a smartphone-based decision tool that will improve admission and referral decision making, reduce the use of broad-spectrum antibiotics (reserving these only for severe pneumonia cases in line with WHO guidelines) and help reduce the problem of antimicrobial resistance (AMR). In order to do so, the two main areas of research are:

1. The development of algorithms that can accurately estimate vital signs using a smartphone camera.
2. The development of machine learning algorithms for the classification of respiratory patterns in children diagnosed with pneumonia.

1.5 Contributions

The major contributions made during my first year of DPhil are:

1. Development of signal processing algorithms to assess the quality of the information recorded by wearable devices and estimate vital signs such as HR, RR and SpO_2 .
2. Development of image and video processing algorithms to extract respiratory and cardiac image plethysmography (PPGi) signals from video data recorded from infants in the Neonatal Intensive Care Unit (NICU). From the physiological signal extracted, I developed algorithms to estimate HR and RR.

1.6 Outline of the report

This report is composed of 5 chapters. Chapter 1 discusses the motivation and objectives of this research. Chapter 2 reviews the background literature and current state-of-the-art technology to diagnose pneumonia. Chapter 3 describes signal processing methods used to compute physiological parameters from wearable devices. Chapter 4 discusses methods used to estimate vital signs from video cameras. Finally, chapter 5 concludes the report and discusses areas of future research work.

Chapter 2

Literature review

2.1 Introduction

Pneumonia is responsible for approximately 18% of deaths in children under the age of five (see figure 2.1). More than 95% of the childhood pneumonia cases and 99% of subsequent deaths occur in low and middle income countries (LMIC)[44]. However, only 3% of global infectious disease research spending is currently allocated to pneumonia [54], such studies being very rare in LMICs due to their resource-intensiveness.

Accurate and timely diagnosis of pneumonia is essential for the prevention of hospitalisation and reduction of mortality rates however, access to high-quality healthcare is often limited in LMICs. Appropriate diagnostic assessment of childhood pneumonia typically relies on the use of advanced tools (such as X-rays and blood culture) by a clinical expert who assesses and interprets a combination of clinical measurements [21]. This chapter reviews existing diagnostic innovations for childhood pneumonia. These approaches include image based technologies that can accurately identify abnormal breathing patterns and data-driven machine learning algorithms for interpretation of symptoms.

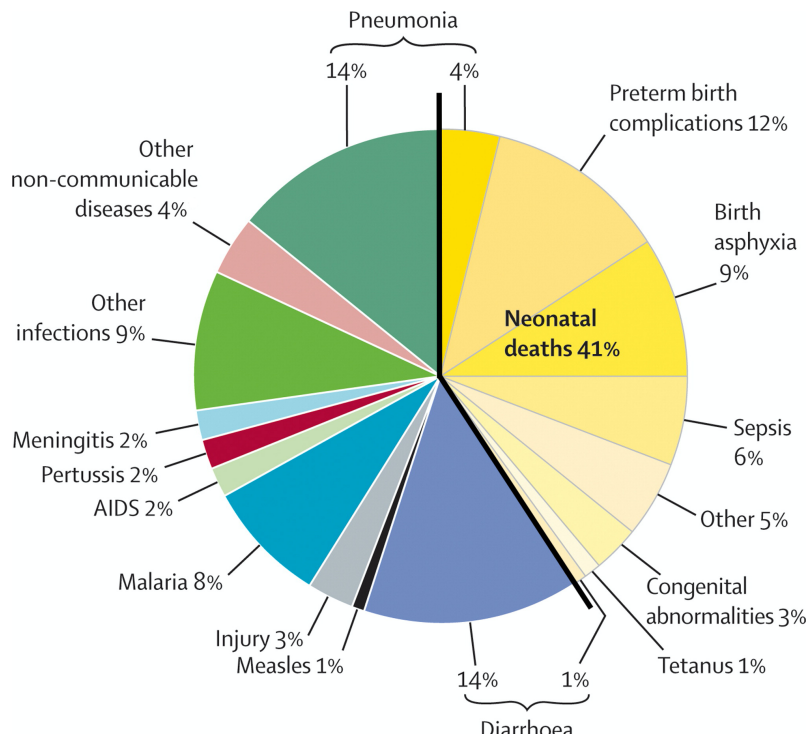


Figure 2.1: Global causes of childhood deaths. Yellow colour represents deaths of neonates aged 0 - 27 days and the rest correspond to children aged 1 month to 5 years [7].

2.2 Diagnostic Innovations

2.2.1 Pulse oximetry

Pulse oximetry is a low-cost technology, widely accepted as the standard for detection of hypoxaemia, an often fatal complication of pneumonia. It has been used to reliably measure hypoxaemia, identifying 20–30% more cases than clinical signs alone [13]. Pulse oximeters are devices that non-invasively measure peripheral oxygen saturation SpO_2 . They are inexpensive, portable and, with adequate training and supervision, can be reliably used with children at all levels of the health system in low-resource settings, including by lay community health workers at the household level [20]. Oxygen saturation estimates may lead to detection of changes in patient conditions that could otherwise be missed, such as a lower $SpO_2 (<95\%)$ which indicates hypoxia and insufficient oxygen supply to the human body. Children with hypoxaemic pneumonia therefore need to be identified, admitted to hospital, given supplemental oxygen and be monitored closely. This necessitates a heightened awareness of the prevalence and the risk of hypoxaemia among children presenting to health-care facilities and robust mechanisms to detect it [49].

2.2.2 Lung auscultation

Lung auscultation is the use of a stethoscope to acoustically assess airflow through the trachea-bronchial tree and remains an important component of pneumonia diagnosis, with more predictive accuracy than an initial clinical assessment alone [43]. The addition of lung auscultation as a diagnostic tool improved the classification of radiographically confirmed clinical pneumonia in cases with decreased breath sounds, absence of wheezes, but presence of crackles [43]. Crackles are discontinuous, explosive, and non musical adventitious lung sounds normally heard in inspiration and sometimes during expiration. Crackles are usually classified as fine or coarse based on their duration, loudness, pitch, timing in the respiratory cycle, and relationship to coughing and changing body position[46]. Although traditional acoustic stethoscopes are inexpensive and portable, the implementation of lung auscultation in low-resource settings is limited by challenges including the training required to recognise the specific signals necessary to make a diagnosis. Computerised analysis of lung sounds has been suggested and explored as a tool for automated classification of acoustic patterns and different respiratory conditions.

2.2.3 Other innovations

Other diagnostic innovations being developed include automated respiratory rate counters with a variety of technologies such as accelerometers and bioimpedance among others). The combination of several diagnostic and prognostic innovations into an integrated instrument could improve identification of pneumonia and its severity [17]. Table 2.1 summarises some of the recent devices proposed.

2.3 Vital sign acquisition and estimation

Respiratory rate can be difficult to measure in a standardised way. It is typically counted manually in low-resource settings, using timers or counting beads. Manual measurement, although often the reference standard, can be imprecise and is affected by intra-observer variation as it requires focused concentration. It is often required to be measured from a crying, irritable and moving child. Automated devices to compute RR are more commonly available in well-resourced settings. These include extracting respiration from the photoplethysmography (PPG) signal from a pulse oximeter, or remotely using a modern camera.

Table 2.1: Summary of diagnostic innovations that have been recently developed, or are currently under development in the context of childhood pneumonia. sources (UNICEF 2013) and personal research.

Diagnostic Innovation		Description
mPneumonia		An Android mobile application which automates the WHO IMCI protocol. The app paired with a software-based breath counter and a pediatric pulse oximeter to facilitate rapid identification of fast breathing [18].
WHO timer and Counting Beads	ARI	Designed as a simple and cheap way to help community health workers count breaths. The counting beads comprise of one strand of beads, non-specific for children ages 0–5 years. The strand is necklace shaped and has a protruding start/end bead. The health worker count breaths by moving a bead for each breath. When 1 minute has passed the CHW counts back the beads to determine the RR. Counting beads should be used in conjunction with the ARI Timer.
RRate mobile application		RRate measures RR by recording the time interval in between breaths as the user taps on a touch sensitive screen of a mobile device in time with inspiration. Once a consistent set of taps has been achieved, a chime noise is played and the result displayed [28].
Amplified stethoscopes e.g ThinkLabs & Ekuore		Digital stethoscopes that can transmit lung signals (auscultation) onto a smart phone [38].
The HealthPatch MD		Consists of two ECG electrodes, a tri-axial accelerometer, micro-controller and transceiver within a patch that straps like a bandage over the heart. The device measures HR, RR, steps and posture and connects wirelessly to a smartphone via bluetooth [9].

2.3.1 Pulse oximetry

One of the earliest light-based continuous vital-sign monitoring methods developed was pulse oximetry, first explored in the 1930s [14]. Pulse oximetry is a non-invasive technology that uses a light source and a photo detector at the surface of skin to measure the volumetric variations of blood circulation. The light source illuminates the tissue, and the photo detector measures the small variations in the reflected or transmitted light intensity associated with changes in perfusion. The fundamental principle of pulse oximetry relies on the differences in absorption of blood and other tissue components at different wavelengths[57]. When the heart pumps blood to the body and the lungs during systole, the amount of blood that reaches the capillaries in the skin surface increases, resulting in more light absorption. The blood then travels back to the heart through the venous network, leading to a decrease of blood volume in the capillaries and less light absorption[50]. These changes can be recorded as the PPG waveform, comprising a pulsatile signal from which oxygen saturation (SpO_2) and other vital signs such as heart rate (HR) and respiratory rate (RR) can be computed.

The pulsatile changes of the PPG waveform is often called the "AC" component, it is synchronous with the beating heart. In contrast, the non-pulsating component "DC" is a function of the basic blood volume, respiration, the sympathetic nervous system, and thermo-regulation. As shown schematically in figure 2.2, most of the signal is static (DC) and represents the light that has not been modulated by arterial blood [35].

2.3.2 Wearable technology

There is a growing interest in continuous monitoring of vital signs outside of traditional settings such as the clinic or hospital. The development of wearable technology that unobtrusively and reliably monitors vital

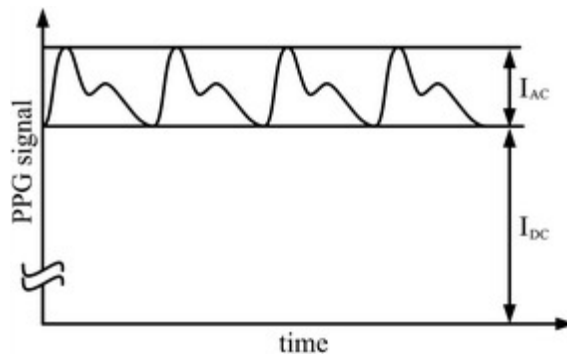


Figure 2.2: A typical PPG waveform showing the AC component and DC component [23]

signs has allowed the evaluation of patient recovery after discharge and the monitoring of those deemed at risk or suffering from chronic illness [8]. Wearable devices can incorporate a range of sensors such as PPG, accelerometer and gyroscopes. These devices can be worn in a variety of different locations, including finger, ear lobe and wrist to provide measurements from these sensors.

2.3.3 PPG imaging

Despite conventional PPG's wide range of applications, there are several significant limitations to the usefulness. Current monitoring systems available to track changes in the vital signs of patients require contact with the subject by using adhesive electrodes or sensors [60]. These can however damage the fragile skin of young infants or cause stress and discomfort. The introduction of fast digital cameras into clinical imaging monitoring and diagnosis systems, the desire to reduce the physical restrictions, and the possible new insights that might come from perfusion imaging and mapping inspired the evolution of conventional PPG technology to photoplethysmographic imaging (PPGi) [50]. Video-based vital sign monitoring extends the concepts of traditional PPG, using the multiple photosites present in an imaging sensor to record the blood volume changes associated with the cardiac cycle. These physiological changes result in a signal from which vital signs such as HR, RR, oxygen saturation SpO_2 and others can be estimated [53, 59].

In 2008, Verkruyse *et al*[58] showed for the first time, that PPG signals could be remotely acquired from the human face with a simple, digital, consumer-level camera as the detector more than 1 m away. The study conducted used daylight as the illumination source in combination with normal artificial fluorescent light. Regions of interest (ROIs) were selected in images of the faces from human volunteers. The authors presented evidence that the reflectance signals were pulsatile cardiac signals by showing that signals corresponding to movement of facial areas with no exposed skin (edge of the face and hair above the ear) were not predominantly at the heart rate frequency. The green channel was found to provide the strongest plethysmographic signal amplitude, corresponding to an absorption peak by oxyhaemoglobin, but the red and blue channels were also shown to contain plethysmographic information. The paper showed how heart rate could be extracted from the frequency content of these images using the fast Fourier transform (FFT) for 10s windows, and hinted at how respiratory rate might be computed using an ROI which encompasses the entire face.

In 2010, Tan *et al* presented a real-time vision based respiration monitoring system. The method involved image and signal processing techniques to extract chest and abdominal movement information from a sequence of video images recorded using a single video camera. The system provided a real-time respiration signal from which RR was computed [52]. In the same year, Bai *et al*[4] designed an embedded

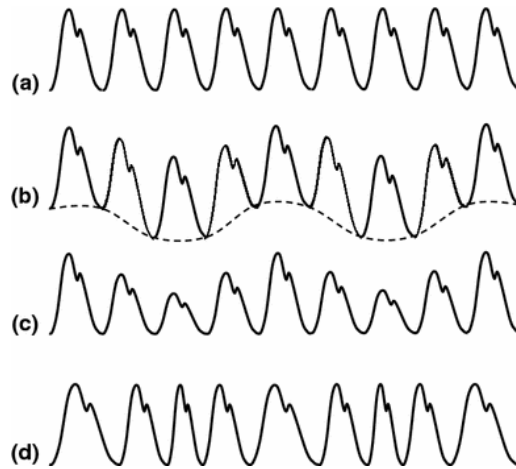


Figure 2.3: Modulation of the PPG signal due to respiration; a) Unmodulated PPG showing cardiac pulse waveforms; b) Baseline modulation (cardiac pulses riding on top of baseline shown dashed); c) Amplitude modulation (cardiac pulse amplitudes varying over the respiratory cycle); d) RSA (pulse period varying over the respiratory cycle). Figure reproduced from [1].

monitoring system for body breath detection using a webcam. Their design employed a temporal differencing algorithm, which subtracts subsequent frames to detect moving objects [30]. This was used to identify chest movement and determine the respiratory rate. The developed system estimated the respiration rate of sleeping or stationary subjects with a static background, which poses a limitation for monitoring children or infants.

Jorge *et al* proposed a new method for use in neonates in 2017, which was incorporated into a Cessation Of Breathing Events (COBE) detection system. For this method, skin pixels were identified first in each frame using a skin classifier and the ROI for motion analysis selected. Motion analysis was done to detect breathing movements and estimate their frequency. A binary signal quality index (SQL) was produced for these estimates based on the level of activity on the video sequence. In contrast to the previous methods discussed, this approach is able to account for subject motion and changes in background lighting [27].

2.4 Respiratory signal processing

2.4.1 Respiratory signal extraction

Extracting a respiratory signal from PPG requires the identification of respiratory modulation components driven by the fluctuation of blood volume in the peripheral vascular bed. These modulation components are pulse amplitude, baseline and respiratory sinus arrhythmia (RSA).

- **Baseline modulation:** A baseline modulation of the PPG signal is caused by changes in venous return secondary to changes in intra-thoracic pressure throughout the respiratory cycle. During inspiration, decreases in intra-thoracic pressure result in a small decrease in central venous pressure increasing venous return. The opposite occurs during expiration. As more blood is averted from the low pressure venous system and the venous bed cyclically fills and drains, the baseline PPG is modulated accordingly [1]. This effect is shown in figure 2.3b.
- **Amplitude modulation:** Amplitude modulation is caused directly by changes in intra-thoracic pressure during the respiratory cycle. These changes result in respiratory oscillations in the amplitude of the

signal, and this effect is shown in figure 2.3c.

- **RSA:** Respiratory sinus arrhythmia is a variation in heart rate that occurs throughout the respiratory cycle. It is well documented that heart rate increases during inspiration and decreases during expiration. While the precise mechanisms of RSA remain disputed, it is a result of autonomic nervous system activity fluctuation during respiration. This effect is shown in figure 2.3d.

The extraction of respiratory components is particularly challenging as the three aforementioned respiratory modulations may be present to varying degrees across the patient population. A further challenge for algorithms to extract respiratory signals is that respiratory components often appear concurrently with a range of other low frequency artefacts due, for example, to voluntary or involuntary movements of the patients or blood pressure changes [1]. Appropriate signal processing techniques must therefore be implemented to accurately extract this information.

2.4.2 Signal processing techniques

From the presence of the respiratory response in a PPG waveform, many researchers have been motivated to develop or utilise methods for RR estimation, such as digital filters, auto-regressive (AR) models, variable frequency complex demodulation and particle filters.

Digital filtering

In their 2000 study, Nilsson *et al* [39] extracted the respiratory synchronous part of the PPG signal using a band pass filter. A 3rd order Butterworth band-pass filter with a pass-band from $f = 0.1 - 0.3$ Hz (6 to 18 breaths/min) was used. Detection of breaths in the filtered PPG signals was done both visually and by using an automated algorithm. In 2009, Nakajima *et al.* developed a technique that used digital filters to estimate HR and RR from a PPG signal. The cut-off frequency of the respiratory signal filter was selected automatically depending on the heart rate so that a higher cut-off frequency was used at higher heart rates [37]. Despite the complexity of the algorithm, it did not perform as well as the method proposed by Nilsson *et al*, and had an average error of over 3 breaths per minute when compared to the reference rate.

Auto-regressive modelling

Auto-regressive (AR) modelling looks for regular frequencies in a signal which is deemed to be stationary over the period of analysis. It models this periodic behaviour by comparing the signal with its own past values at various time lags [51]. In 2007, Fleming and Tarassenko developed a method to estimate RR from a PPG signal using an AR model. This method was shown to perform better than both the digital filtering and wavelet decomposition methods [15]. An AR method involving factorising the estimated AR parameters into multiple pole terms was later presented by Lee *et al* [29]. The pole with the highest magnitude was chosen to represent the respiratory rate. The method showed accurate respiratory rate extraction, especially for high respiratory rates (36 – 48 breaths/min). To mitigate a previously described limitation of AR models, particle filtering was introduced to track moving targets. Recent efforts have been made to develop efficient algorithms for real-time implementation [26].

HR and RR estimation using AR modelling has also been proposed for video-based vital sign monitoring by Tarassenko *et al.* [53]. This method also cancels out aliased frequency components caused by artificial light flicker using AR modelling and pole cancellation.

Chapter 3

Vital sign estimation using wearable devices

3.1 Introduction

Wearable devices such as wristbands and smart watches are increasingly being used to monitor the physiological parameters of individuals to track changes in heart rate, oxygen saturation and respiratory rate [10]. Data can be acquired without imposing a disruption to a subject's daily schedule, providing a more informed assessment of the subject's well-being and helping detect health problems that might have otherwise been missed. The availability and low cost of wearables could therefore provide new ways to monitor children's health in LMICs. The aim of the chapter is to compute HR, RR and changes in SpO_2 from data recorded from a wearable device in a clinical study involving healthy volunteers undergoing a hypoxia protocol.

3.2 Data set

The clinical study took place at the Cardiovascular Clinical Research Facility, John Radcliffe Hospital, Oxford, UK. It was a collaboration between the Institute of Biomedical Engineering and clinicians from the Nuffield Department of Clinical Neurosciences at the University of Oxford. The study received ethical approval by the East of Scotland Research Ethics Service REC 2 (19/ES/0008). The study was carried out to test the performance of wearable devices in a simulated clinical setting during hypoxia exposure (low oxygen levels).

3.2.1 Participant recruitment and assessment

43 healthy volunteers were recruited for the study. Written consent was obtained for each study participant. The screening assessment for the study was completed by an appropriately qualified, medically trained member of the research team, who confirmed the volunteers' eligibility. Participants were excluded if incomplete data were collected for any one device during the duration of the study, or if hypoxia was not achieved.

Demographics data including age, sex, height, weight, skin type (Fitzpatrick scale [25]), heart rate and SaO_2 (from arterial blood gas (ABG)) were collected for each participant, at the start of their sessions and recorded in a Case Report Form (CRF). All data from participants were identified using a study number. Four participants presented adverse clinical conditions (three anaemia cases - evaluated from the first ABG - and one sickle cell trait). Therefore, 39 complete data sets were acquired in total. The summary of the demographic information of the study volunteers is presented in table 3.1.

3.2.2 Study set-up

The study participants lied comfortably on a bed in a semi-horizontal, supine position. A tight-fitting silicone face mask was placed and connected to a hypoxic unit (Everest Summit Hypoxic Generator). If required, additional 7% oxygen in nitrogen from a cylinder was added into the hypoxic circuit to ensure tight

Table 3.1: Summary of the population in the clinical study.

Description	Value
Total number of complete recording sessions	39
Average length of a recording session (minutes)	18.4 ± 2.9^1
Gender	
Females	21 (53.8%) ²
Male	18 (46.2%) ²
Age	32.6 ± 10.4^1
Weight	71.2 ± 13.4^1
Height(m)	1.71 ± 0.10^1
Fitzpatrick Skin type	
Type I	10 (25.6 %) ²
Type II	18 (46.2 %) ²
Type III	2 (5.1 %) ²
Type IV	9 (23.1 %) ²

¹ mean \pm standard deviation² Total number (percentage)

control of fraction of inspired oxygen (FiO_2) provided to the participant. SaO_2 readings were taken for the 100%, 95%, 90%, 87%, 85%, 83% and 80% SpO_2 target values, with the corresponding output of the blood gas analyser then taken as the reference value. SpO_2 stability was subjective for each target SaO_2 window, i.e. a senior anaesthetist decided when a stable oxygen level was achieved in order to take the ABG, based on the clinical values shown by the standard SpO_2 monitor. SpO_2 measurements of greater than or equal to 90% were considered normoxia, while levels between 85% and 89% were considered mild hypoxia. Oxygen saturation levels below 85% were regarded as severe hypoxia.

3.2.3 Instrumentation

Participants wore several ambulatory monitoring devices (AMD) including a purely wrist worn device (Wavelet Health, USA) and up to three wrist-worn devices with finger probes. In this chapter, data from the Wavelet wristband, wearable device using reflectance PPG to measure pulse rate was used. The device records 1 minute red and near-infrared (NIR) time series data with 1 minute gaps in between at a sampling rate of 79Hz. Other sensors in the Wavelet Health include 3-axis accelerometer sensor (recorded at 10Hz) and gyroscope.

The Philips Monitor MX450 was used as the reference clinical standard device, recording SpO_2 values and HR at a sample rate of 1Hz. Figure 3.1 shows a 30-minute window of vital signs measured using the Philips monitor, as well as the red/NIR signals recorded from the Wavelet Health device.

3.2.4 Data selection

39 complete data sets were acquired. 28 sessions with data that was greater than 20 minutes in length were selected; to allow 2 minutes for recovery to normal oxygen saturation (>90%). 19 sessions were subsequently selected because these data sets were not corrupted by motion. Finally 10 sessions were selected for analysis in this report. Figure 3.2 shows a summary of the data collection criteria.

Figure 3.3 shows the distribution of HR, SpO_2 and RR values from the 10 chosen volunteers. Mean $\text{SpO}_2 = 91.2\%$, Median $\text{SpO}_2 = 90.9\%$, Inter-quartile range = 13.9. The mean HR was 66.3 beats/minutes.

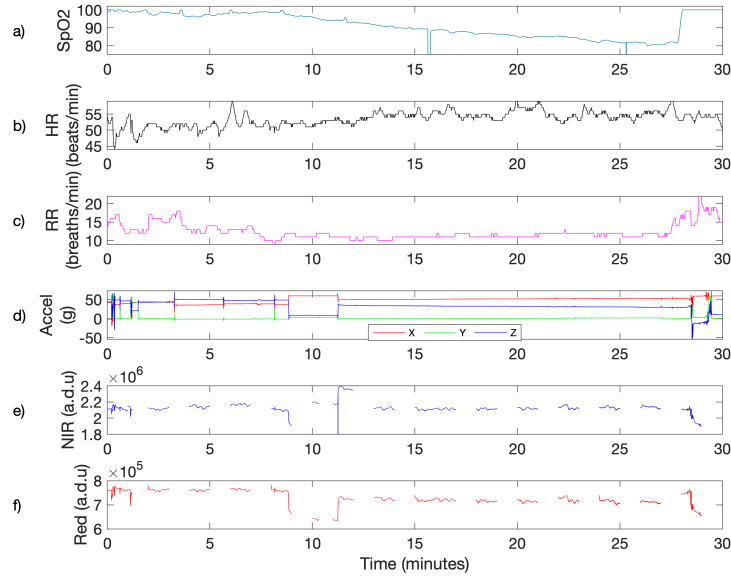


Figure 3.1: Physiological parameters recorded by the Phillips monitor and the Wavelet Health device. a) SpO_2 from the Phillips monitor. Lowest recorded Oxygen saturation was 80% as per protocol. b) Heart rate and c) Respiratory rate from the Philips monitor. d) Accelerometer data recorded by Wavelet Health. e) Raw NIR signal and f) Red signal from the Wavelet Health device. The device records 1 minute data on and off.



Figure 3.2: Flow diagram outlining the patient selection process.

Median HR = 65 beats/minutes, inter-quartile range = 12. Mean RR = 14.1 breaths/minutes, Median RR = 14 breaths/minutes, Inter-quartile range = 55.

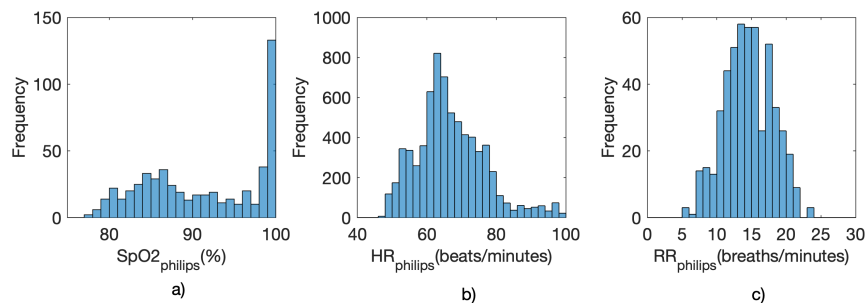


Figure 3.3: Distribution of vital signs recorded by the Philips monitor for the 10 sessions selected for analysis. a) SpO_2 ; b) HR and c) RR

3.3 Heart rate estimation

3.3.1 Overview of the process

HR is used frequently in healthcare and easily extractable from a PPG signal, as pulsatile blood flow from the heart modifies the absorption of NIR light. The NIR signal was detrended and filtered to remove noise. The filtered signal was then split into 10s windows, and the peaks of the pulsatile signal were detected for each of these windows. These peaks were counted to estimate HR. A motion SQI was then applied using accelerometer data from the Wavelet Health device, which discarded HR estimates where the NIR signal was corrupted by motion. Figure 3.4 presents an overview of the process of estimating HR using the Wavelet Health device.

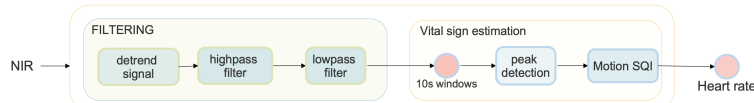


Figure 3.4: Flow diagram outlining the process of computing heart rate from the NIR signal from the Wavelet Health device.

3.3.2 Filtering

The NIR signal was first detrended to remove the DC component. The de-trended signal was further processed by designing two zero-phase FIR filters, shown in figure 3.5, to remove low and high frequency noise from the signal respectively. A 181st order high-pass filter was designed with a passband frequency of 0.7Hz (42 beats/min) and a stop-band frequency of 0.3Hz (18 beats/min). A 36th order low-pass filter was subsequently applied with a passband frequency of 2Hz (120 beats/min) and a stop-band frequency of 4Hz (240 beats/min). Both filters were designed with a passband ripple of 1dB and stop band attenuation of 20dB.

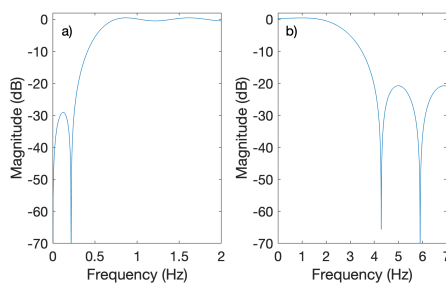


Figure 3.5: Magnitude responses for a) High-pass filter b) low-pass filter.

Figure 3.6 shows an example plot of the NIR signal before and after de-trending and filtering. The Fast Fourier Transform (FFT) plots shown in figure 3.6c and figure 3.6d show a clear peak at 0.9 Hz corresponding to a HR of approximately 54 beats/minute. The reference HR recorded by the Philips monitor was 55 beats/minute.

3.3.3 Peak detection

Peak-to-trough analysis was performed on the filtered signal. This process identified prominent maximum and minimum points in the signal to measure changes in signal amplitude. The algorithm used for peak detection first identified a peak as the i_{th} sample in a time series ts if:

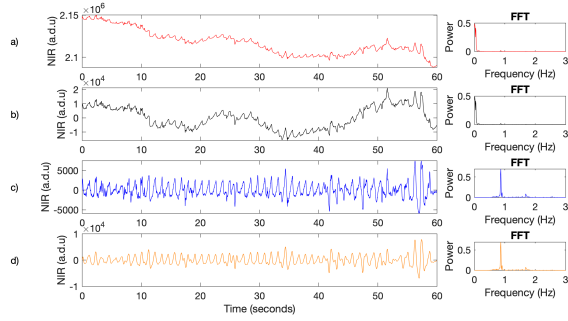


Figure 3.6: 60-second sample time series from the NIR waveform. a) Input signal; b) de-trended. Signal after the c) high-pass and d) low-pass filter were applied. The FFT panels show a peak at 0.9Hz corresponding to a HR of approximately 54 beats/minute. The reference HR recorded by the Philips monitor was 55 beats/minute.

$$ts(i) > ts(i - 1) \text{ and } ts(i) > ts(i + 1) \quad (3.1)$$

To avoid reporting erroneous peaks due to noise, identified peaks were kept if:

$$ts(i_{peak}) > MinPeakHeight \quad (3.2)$$

where *MinPeakHeight* was set to a signal intensity of 100, based on manually observing the minimum height of waveform peaks in low intensity segments of the recording. Remaining peaks were retained if:

$$i_{peak_n} - i_{peak_{n-1}} > MinPeakDistance \quad (3.3)$$

where *MinPeakDistance* was set to give a refractory period (a recovery time after each peak) of 40 samples (corresponding to 84 beats/minute) based on the histogram of reference vital-sign data for the session in figure 3.3. Finally, peaks were selected as:

$$prom(i_{peak}) > MinPeakProminence \quad (3.4)$$

where *prom* was the prominence of a peak, defined as the height of the peak relative to neighbouring troughs. Here, *MinPeakProminence* was set to a value of 58 based on manually observing peak prominences in several example recording segments. The algorithm then returned a vector containing the location and magnitude of each peak as shown in figure 3.7.

3.3.4 Motion SQI

Motion analysis was used to compute a signal quality index (SQI) designed to exclude time periods during which significant movement artefacts occurred. The accelerometer data recorded by the Wavelet health device was first split into 5-minute non-overlapping windows. Subsequently, the mean and standard deviation were calculated for each window. Data points for which the acceleration was greater than ± 2 standard deviations from the mean for that window were considered to have an SQI of 0, corresponding to

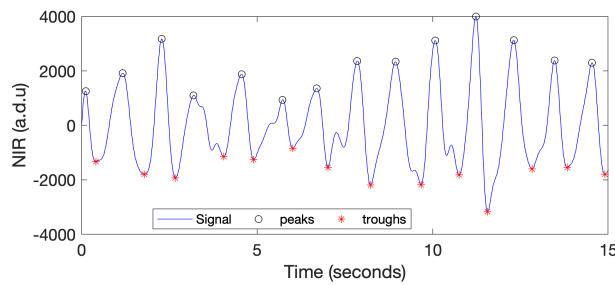


Figure 3.7: Detection of peaks and troughs on the NIR signal over a 15-second sample window.

time periods of motion; otherwise an SQI of 1 was assigned, corresponding to time periods of good quality. Finally, the NIR signal within ± 3 s of any accelerometer data with an SQI of 0 were discarded. An example of this process is shown in figure 3.8.

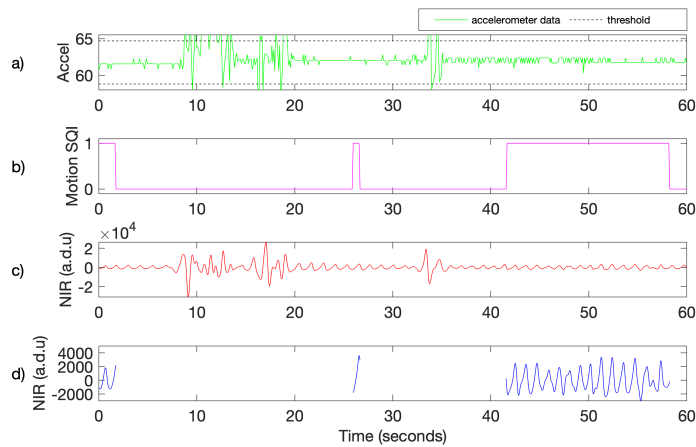


Figure 3.8: Using motion SQI to discard time periods corresponding to motion artefacts. a) Accelerometer data, b) computed SQI, data is discarded at $SQI = 0$. c) NIR signal before motion SQI, d) NIR signal after motion SQI was applied.

3.3.5 Heart rate computation

Beat-to-beat time intervals were computed by subtracting the time value of each peak from the time value of a succeeding peak. From the peak-to-peak intervals, HR was computed using a window length of 10 seconds sliding by 1 second. The averaged values of HR were then calculated using the equation below:

$$HR = \frac{60}{\text{median}(\text{peak_time_interval})} \quad (3.5)$$

3.3.6 Time alignment between heart rate from Philips and HR estimated from the Wavelet Health device

The Wavelet Health and Phillips devices have separate clocks, which could not be synchronised. The time delay between devices varied session to session. To compare vital signs estimated from the Wavelet Health device to reference values from the Phillips monitor, the time delay between these devices need to be estimated and accounted for. This was accomplished by comparing the estimated HR values from the Wavelet device with the reference HR signal from the Phillips monitor, similar to Chaichulee [11]. The cross correlation between the two HR signals was calculated for time lags from -30 s to 30 s.

Given that f and g are vectors containing a time series signal, the cross-correlation measures the similarity between f and a shifted version of g . The cross-correlation at a time lag t is defined as:

$$R_{xy}(t) = \frac{\sum_{i=1}^N (f_i - \mu_f)(g_{i-t} - \mu_g)}{(N-1)\sigma_f\sigma_g} \quad (3.6)$$

where μ_f and μ_g are the means of f and g respectively, σ_f and σ_g are the variances of f and g respectively. The maximum of the cross-correlation indicated the time delay for which the two signals are best aligned. The time delay is defined as

$$T = \text{argmax} R_{xy}(t) \quad (3.7)$$

The time delay indicates how much g is shifted, along the x-axis (time axis), with respect to f . Computed heart rates were then plotted and comparisons were made with the reference heart rate from the Philips monitor.

3.4 Respiratory rate estimation

3.4.1 Overview of the process

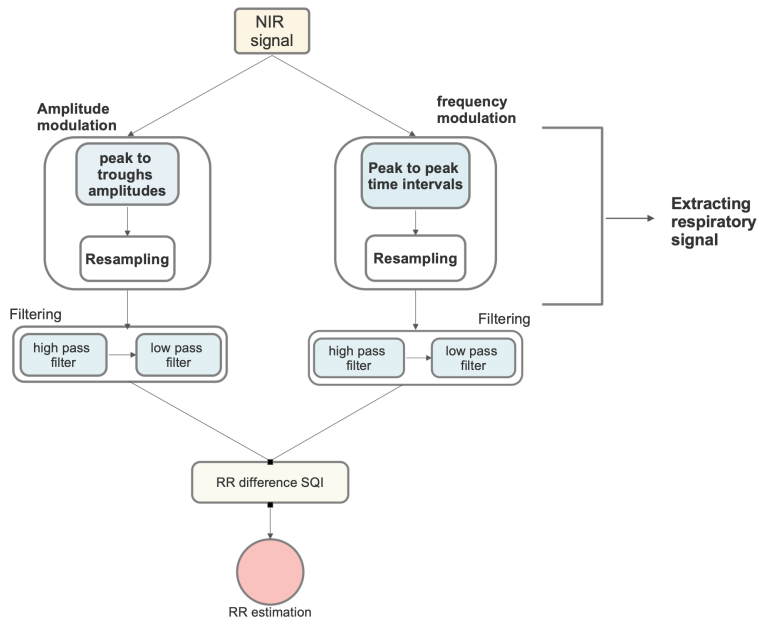


Figure 3.9: Flow diagram outlining the process of computing respiratory rate from the NIR signal recorded by the Wavelet Health wearable device.

The estimation of respiratory rate is possible because the NIR signal recorded by the Wavelet device presents respiratory driven blood volume changes. Modulation of the NIR signal due to respiration is used to estimate RR. Two methods were used to extract a respiratory signal and compute RR from the raw NIR PPG signal. Amplitude modulation, caused by changes in intra-thoracic pressure during the respiratory cycle, resulted in respiratory oscillations in the amplitude of the signal from which RR could be estimated. The second method, frequency modulation, used the variation in the instantaneous heart rate during the respiratory cycle, also known as respiratory-sinus arrhythmia. The extracted respiratory signals were filtered

using two zero-phase Infinite Impulse Response (IIR) filters. The mean of the two filtered respiratory signals was taken as the final estimate of RR.

3.4.2 Extracting respiratory signal

Amplitude modulation

Amplitude modulation is defined as the difference in peak amplitudes of consecutive peaks and troughs, effectively resulting in a time-series of the amplitude of each PPG pulse. It is caused directly by changes in intra-thoracic pressure during the respiratory cycle. These changes result in respiratory oscillations in the amplitude of the signal, from which RR can be estimated. For this method, the peaks and troughs of the NIR signal were computed using the algorithm described in section 3.9, as shown in figure 3.10a. The amplitude of each beat was computed by subtracting the trough values from each respective peak. Outliers, defined as values more than three standard deviations from the mean, were removed from the peak-trough amplitudes to discard noisy periods. The signal was then re-sampled at 25 Hz (using a cubic spline), and de-trended as shown 3.10b and 3.10c.

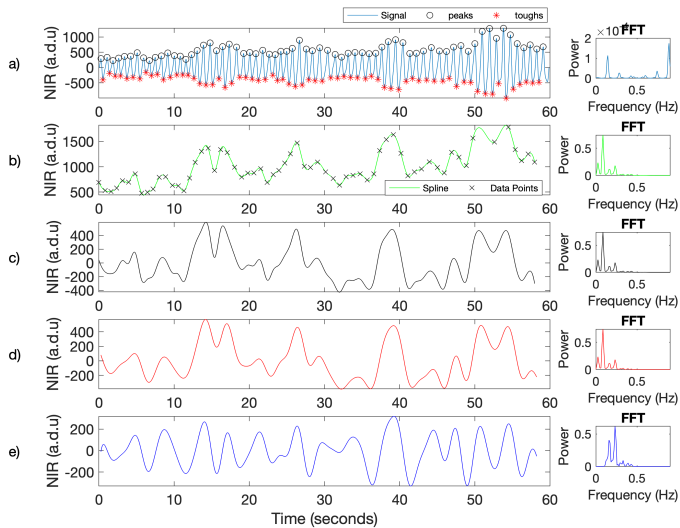


Figure 3.10: 60-second example of the amplitude modulation method being used to estimate RR from the NIR signal. a) Peak-to-trough detection; b) signal amplitude; c) de-trended; d) low-pass filtered signal; e) high-pass filtered signal. The FFT panels show a peak at 0.23Hz, corresponding to a RR of approximately 13.8 breaths/minute. The reference RR recorded by the Philips monitor was 15 breaths/minute.

Two Butterworth IIR filters shown in figure 3.11, were designed to remove low and high frequency noise from the signal. An 8th order low-pass filter was designed with a cut-off frequency of 0.60 Hz (36 breaths/min) and a passband frequency of 0.40 Hz (24 breaths/min). A high-pass filter of order 17 with a passband frequency of 0.12 Hz (7.2 breaths/min) and a cut-off frequency of 0.10 Hz (6 breaths/min) was then applied to the signal. Both filters were designed with a passband ripple of 1 dB and stop band attenuation of 20 dB. Figure 3.10 shows an example plot of the NIR signal before and after de-trending and filtering. The designed filters were used to remove low and high frequency noise from the signal as shown in figure 3.10d and 3.10e.

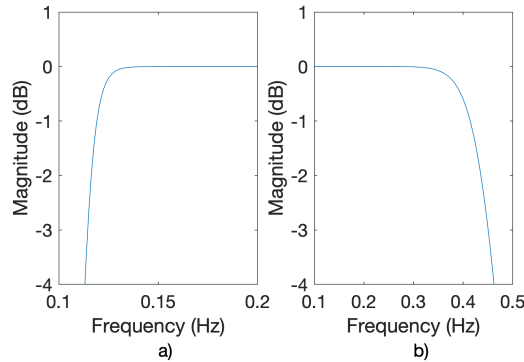


Figure 3.11: Filter magnitude responses for a) high-pass filter b) low-pass filter.

Frequency modulation

Frequency modulation, also known as respiratory sinus arrhythmia, is a variation in heart rate that occurs throughout the respiratory cycle. It is well documented that heart rate increases during inspiration and decreases during expiration. While the precise mechanisms of frequency modulation remain disputed, it is a result of autonomic nervous system activity fluctuation during respiration.

To compute RR using this method, peak to peak time intervals were computed by subtracting the peak time point from a succeeding peak. The peak-to-peak time intervals for each breath pulse from the NIR signal were extracted to construct a respiratory signal. The signal was re-sampled at 25Hz (using a cubic spline). Subsequently, the detrended signal was filtered using similar filters designed for the amplitude modulation method. The peak-to-peak time intervals were then used to compute RR. An example from this process is shown in figure 3.12. The FFT panels show a peak at 0.24Hz, corresponding to a RR of 14.4 breaths/minute. The reference RR recorded by the Philips monitor was 15 breaths/minute.

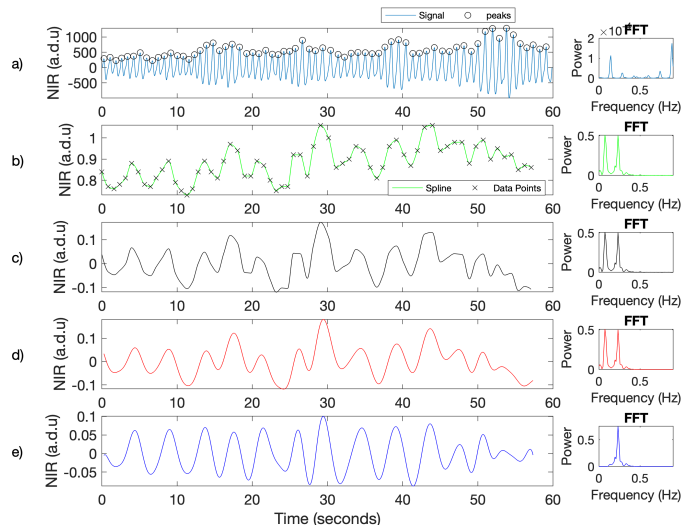


Figure 3.12: 60-second example of the frequency modulation method used to estimate RR from the NIR signal. a) Peak to peak time intervals; b) peak to peak time intervals; c) de-trended; d) low-pass filtered signal; e) high-pass filtered signal. The FFT panels show a peak at 0.24Hz, corresponding to a RR of 14.4 breaths/minute. The reference RR recorded by the Philips monitor was 15 breaths/minute.

3.4.3 RR estimation

To compute RR, similar algorithms described in section 3.3.3 were used to perform peak to peak analysis on the respiratory signals extracted from the NIR waveform using both of the proposed methods. This analysis was done using MinPeakDistance of 1.2 s (50 breaths/min) and MinPeakProminence of 0.02. RR was computed as the average peak-to-peak time interval over a window of 30 seconds sliding by 5 seconds. The agreement between the estimated RR from the two methods (amplitude and frequency modulation) was used to compute an SQI. This SQI was set to 1, corresponding to periods of good quality estimates, if the two estimates were within 5 breaths/min; conversely, it was set to 0 otherwise, corresponding to time periods of poor-quality estimates. The mean of the two respiratory rates was taken as the final estimate of RR for periods of good-quality signal.

3.5 Oxygen saturation

3.5.1 Overview of the process

The Wavelet Health device, although it provided estimates of HR, also recorded the red and NIR signals. These signals were split into windows, and then detrended and filtered to remove noise. Subsequently, a motion SQI was applied using accelerometer data to remove data where the red and NIR signals were corrupted by motion. After this, the peaks and troughs in the red and NIR signals were detected, and the signal amplitude computed. The ratio between the red and NIR signal amplitudes were then compared to the reference SpO_2 estimates from the Philips monitor. This process is shown in figure 3.13.

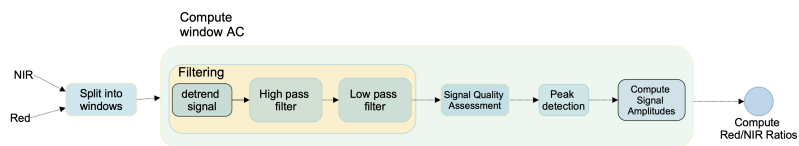


Figure 3.13: Flow diagram outlining the process of computing the relationship between the ratio of ratios of the red and NIR signals recorded by the Wavelet Health device and the reference SpO_2 from the Philips monitor.

3.5.2 Filtering

The NIR and Red signals were de-trended and subsequently filtered using two zero-phase FIR filters with a passband ripple of 1dB and stop band attenuation of 20dB to remove low and high frequency noises from the signal respectively. The high-pass filter was designed with a passband frequency of 0.7Hz (42 beats/min) and a stop-band frequency of 0.3Hz (18 beats/min)). The low-pass filter was designed with a passband frequency of 2Hz (120 beats/min)) and a stop-band frequency of 4Hz (240 beats/min)). Thresholds were selected based on the population distribution of data shown in figure 3.3. The magnitude response of the resulting filters is shown in figure 3.14.

Motion SQI and peak detection algorithms similar to those used in section 3.3 were then applied to the filtered data.

3.5.3 Signal amplitude

The detected peaks and troughs used for HR were used to compute the amplitude of the red and NIR PPG signals. Amplitudes were determined by consistently subtracting the value of a trough from the value of a preceeding peak.

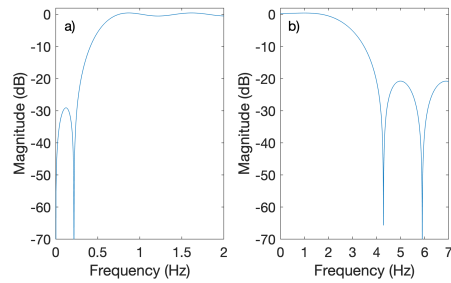


Figure 3.14: Magnitude responses for the a) High-pass filter and b) low-pass filter designed.

3.5.4 Computing Red/NIR Ratios

Median values of the red and NIR PPG amplitudes were computed for non-overlapping windows of length 15 second and with 15 second step size. The ratio between the red and NIR PPG amplitudes was then applied. For comparison, the median of 15 second non-overlapping windows were also computed from the reference SpO_2 values recorded by the Philips monitor data. The computed Red/NIR ratios were then compared to the median SpO_2 values to assess the correlation.

3.6 Results

3.6.1 Error metrics

The comparison between the reference values from the Philips monitor and the estimated vital signs from the Red and NIR signals for all recordings in the study were performed using Bland-Altman analysis, the mean absolute error (MAE), the mean absolute deviation (MAD) and Pearson's correlation coefficients. The Bland-Altman plot was designed to assess the agreement between two measurements. It was constructed by plotting the mean of the estimates from the devices against their differences.

Given two time series x and y of length N , the MAE was defined as:

$$MAE = \frac{1}{N} \sum_{i=1}^N |y - x| \quad (3.8)$$

Given z is the difference between the two time series x and y , and μ is the mean of z , the MAD was defined as:

$$MAD = \frac{1}{N} \sum_{i=1}^N |z - u| \quad (3.9)$$

The Root Mean square error (RMSE) was calculated using the equation

$$RMSE = \sqrt{\frac{1}{N} \sum_{i=1}^N (y - x)^2} \quad (3.10)$$

The Pearson's correlation coefficient measures the linear correlation between two time series using the following equation:

$$R = \frac{\text{cov}(x, y)}{\sigma_x \times \sigma_y} \quad (3.11)$$

where $\text{cov}(x, y)$ is the covariance, σ_x and σ_y are the standard deviation of x and y time series respectively.

3.6.2 Heart rate

Figure 3.15 compares the reference HR from the Philips monitor with the estimated HR from the Wavelet Health device. Table 3.2 shows MAE, MAD, RMSE values and the correlation values computed across the 10 subjects selected for analysis.

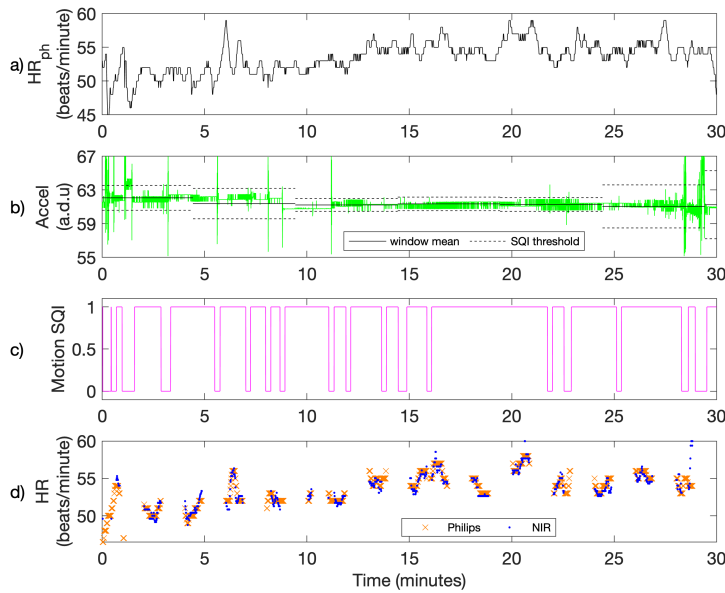


Figure 3.15: Comparison between HR provided by the Philips monitor and the HR estimates computed by the proposed algorithms. a) HR from Philips monitor. b) Accelerometer data recorded by the Wavelet Health device. c) Motion SQI. Values of 1 correspond to periods of good-quality signal; Conversely values of 0 correspond to periods of poor quality signal. d) Estimated HR from NIR signal compared to reference HR.

Table 3.2: Summary of results for the proposed algorithms to estimate HR from the NIR signals for the 10 patients analysed.

Patient Number	MAE*	MAD*	RMSE*	r
001	0.6	0.6	0.9	0.92
002	1.6	1.6	2.0	0.94
003	0.6	0.6	0.8	0.99
004	1.0	1.0	1.3	0.98
005	0.7	0.7	1.0	0.98
006	1.9	1.9	2.9	0.89
007	1.2	1.2	1.8	0.97
008	2.3	2.2	3.1	0.9
009	0.7	0.7	1.0	0.96
010	1.2	1.2	1.5	0.97
Overall	1.2	1.2	1.8	0.99

*Values in beats/minute

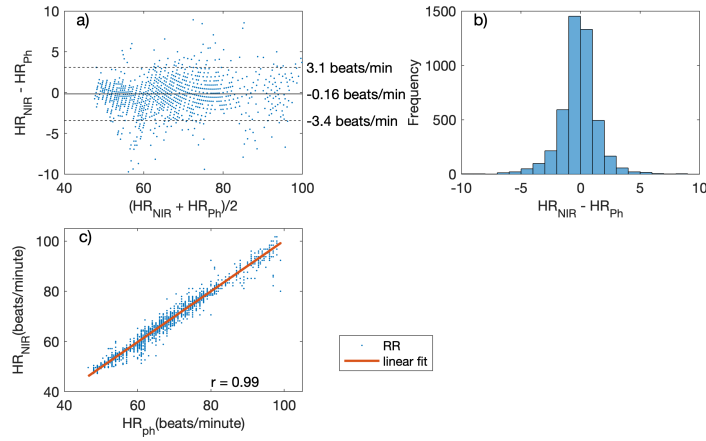


Figure 3.16: Comparison between the reference and estimated heart rate for the 10 patients analysed. a) Bland-Altman plot, b) histogram of the differences between the two heart rate estimates. c) Correlation plot showing a positive correlation between the two measurements, the red line represents the linear fit.

Figure 3.16 (a) shows the Bland- Altman plot comparing the Philips and estimated heart rate values for all 10 patients. The plot shows a mean bias of 0.16 beats/min, 95% of the differences fall within [-3.4, 3.1] beats/min, the correlation coefficient is 0.99. The MAE between both heart rate measurements was 1.2 beats/min with a MAD of 1.2 beats/min.

3.6.3 Respiratory rate

Figure 3.17 shows a comparison between the reference RR from the Philips monitor and the estimated RR computed from the Wavelet Health device by the proposed algorithms. Table 3.3 shows MAE, MAD and RMSE values, correlation values and the error distribution computed across 10 subjects in the dataset.

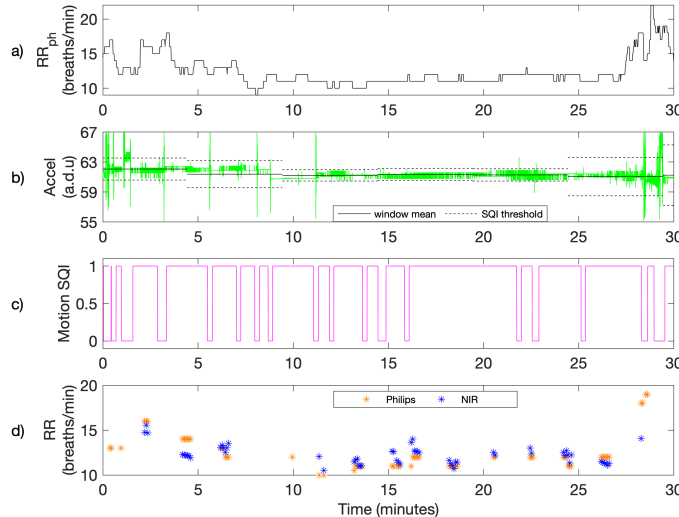


Figure 3.17: Comparison between the reference RR provided by the Philips monitor and the estimated respiratory rates a) RR from Philips monitor; b) Acceleration data from the Wavelet Health device; c) Motion SQL. Values of 1 correspond to periods of good-quality signal; Conversely values of 0 correspond to periods of poor quality signal; d) RR medians computed from reference respiratory rate and computed respiratory rate from the NIR signal.

Table 3.3: Summary of the results for the proposed algorithms to estimate respiratory rate.

Patient No.	Amplitude modulation				Frequency Modulation				Combined Method			
	MAE*	MAD*	RMSE*	r	MAE*	MAD*	RMSE*	r	MAE*	MAD*	RMSE*	r
001	1.4	1.4	2.0	0.33	1.4	1.4	2.0	0.60	0.9	0.9	1.2	0.61
002	2.7	2.0	3.6	0.45	2.2	1.9	2.9	0.54	1.7	1.3	2.2	0.74
003	2.5	2.2	3.5	0.27	3.0	2.8	4.5	0.09	1.0	1.0	1.5	0.79
004	1.9	1.8	2.5	0.19	1.4	1.4	1.9	0.51	1.5	1.4	2.0	0.42
005	1.4	1.3	1.7	0.55	2.4	1.8	3.0	0.53	1.4	1.2	1.8	0.57
006	4.0	2.9	5.0	-0.32	2.3	2.0	3.0	0.06	2.5	2.4	3.6	-0.17
007	3.7	2.8	4.5	-0.05	1.8	1.8	2.5	0.08	2.0	2.0	2.5	0.11
008	3.6	2.2	4.6	0.08	4.4	2.7	5.3	0.17	3.4	2.0	4.1	0.19
009	1.4	1.2	1.8	0.36	4.2	3.7	5.6	-0.16	0.8	0.8	1.0	0.46
010	2.6	3.2	4.2	0.34	1.2	1.3	3.3	-0.09	0.6	0.6	0.8	0.89
Overall	2.5	2.5	3.5	0.52	2.3	2.3	3.5	0.47	1.6	1.6	2.3	0.74

*Values in breaths/minute

Figure 3.18(a) shows the Bland- Altman plot comparing the Philips and estimated respiratory rate values for all 10 patients. The plot shows a mean bias of 0.18 breaths/min, most of the differences falling within [-4.3, 4.6] breaths/min, the correlation coefficient is 0.74. The MAE between both respiratory rate measurements was 1.6 breaths/min with a MAD of 1.6 breaths/min.

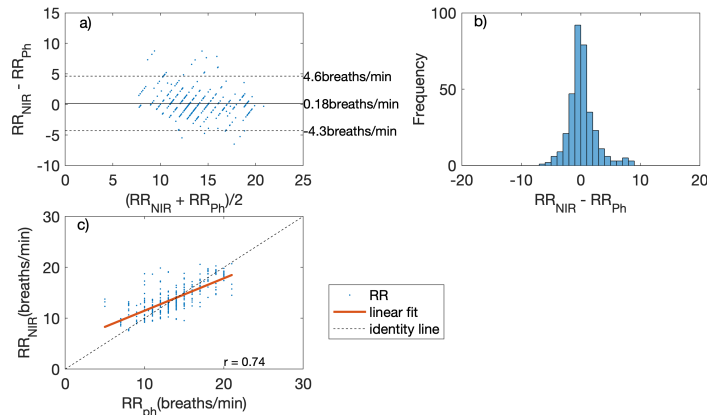


Figure 3.18: Comparison between the reference and estimated RR for the 10 patients in the dataset. a) Bland-Altman plot; b) histogram of the differences between the two RR estimates; c) Correlation plot shows a positive correlation between the two measurements, the red line represents the linear fit.

3.6.4 SpO_2

Figure 3.19 shows the relationship between the ratio of ratios computed using the Red/NIR signals from the Wavelet Health wearable device, compared with the reference SpO_2 provided by the Philips monitor for a sample recorded session. An inverse correlation between SpO_2 and the Red/NIR ratio can be seen. Figure 3.20 shows the scatter plots comparing the red/NIR ratio obtained from the Wavelet Health to the Philips SpO_2 values for all 10 patients. The plots shows correlation coefficient ranging from $r = 0.62$ to $r = 0.98$.

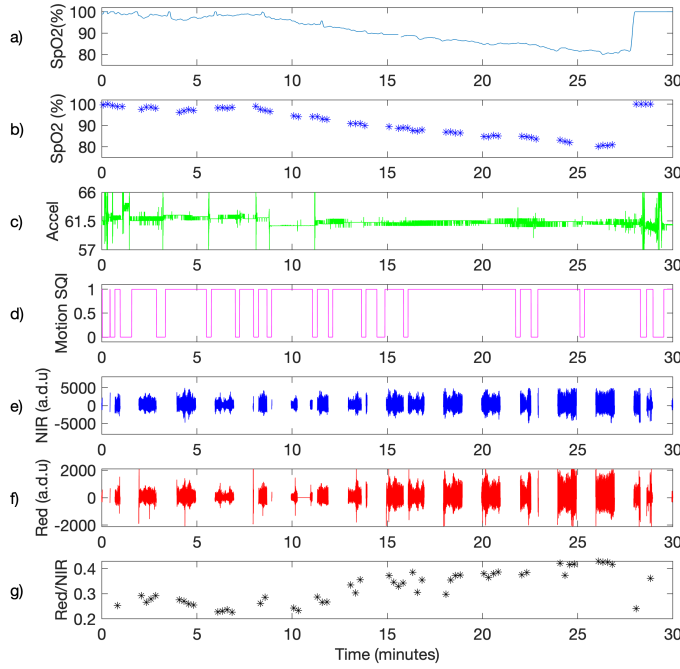


Figure 3.19: Comparison of the trend between the Red/NIR ratio and the reference SpO_2 . a) Reference SpO_2 ; b) Medians of the reference SpO_2 ; c) Accelerometer data; d) Motion SQL; e) NIR signal amplitudes; f) Red signal amplitudes; g) Red/NIR amplitudes ratio.

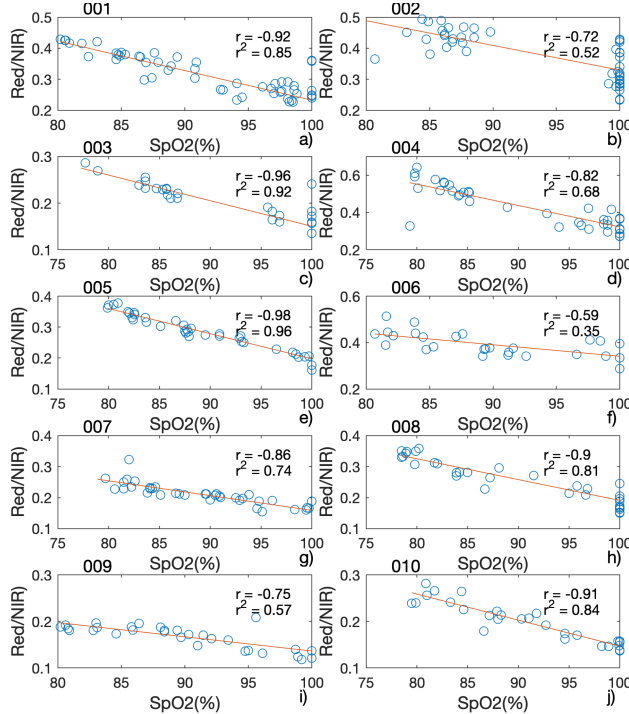


Figure 3.20: Correlation plots of the Red/NIR Ratio for the 10 patients in the dataset. Increased red light absorbance (increased ratio) is associated with increased de-oxyhaemoglobin, i.e., lower SpO_2 . The red line represents the linear fit.

3.7 Discussion

Heart rate is a vital sign that can be estimated from a wearable device, which makes it a good candidate for validating the proposed signal processing algorithms. As can be seen in figure 3.16 and table 3.2, our HR estimates are comparable to the values computed by a reference medical device. The mean bias of 0.16 beats/min and correlation coefficient of 0.99 suggests that our proposed signal processing algorithms work adequately.

Respiratory rate is considerably more difficult to estimate from a wearable device. The lower correlation coefficient ($r = 0.74$) and errors (MAE and MAD of 1.6 breaths/min) shown in figure 3.18 and table 3.3 respectively, are clear indication of this. By combining the two proposed methods using an additional SQI (respiratory difference) the estimation results were improved and there was a low bias and positive correlation present.

The Wavelet Health device is a novel wrist worn device. Comparisons between SpO_2 from the Philips monitor and Wavelet Health device showed inconsistent performance showing that the device is not adequate to estimate SpO_2 during desaturation periods.

3.8 Conclusion

This chapter presented the algorithms for estimating vital signs (HR,RR and SpO_2) from the Wavelet Health wearable device. The HR results had minimal errors with a positive correlation coefficient of 0.99. The other results (RR and SpO_2) had errors greater than the WHO guidelines. New and improved methods are needed to design technologies that can estimate vital signs for the target population of this report

Chapter 4

Non-contact estimation of vital signs

4.1 Introduction

The introduction of digital cameras into clinical image monitoring and diagnosis systems has allowed for tracking of changes in the vital signs of patients without contact with the individual. Though a great development, most existing studies in video-based non-contact vital sign monitoring have been carried out in tightly controlled conditions, over short periods of time (typically up to a couple of minutes). Furthermore, most current algorithms require a person to be still to ensure reliable measurements. The robustness of methods for estimating vital signs is therefore challenged when processing video data recorded from patients under real-life conditions.

4.2 Dataset

The clinical study used to obtain data was part of a research programme in the Oxford University Hospitals NHS (National Health Service) Foundation Trust and the Oxford Biomedical Research Centre (BRC). For this study, pre-term infants (born at less than 37 weeks of gestation) were nursed in a designated study incubator in the high-dependency area of the Neonatal Intensive Care Unit (NICU) at the John Radcliffe Hospital in Oxford. The clinical team recruited the infants based on the British Association of Perinatal Medicine's Categories of Care 2011.

30 pre-term infants were monitored for up to four consecutive days without affecting regular patient care. The participants were double-monitored with a digital video camera and the standard patient monitoring devices. The study was performed during daytime under regular ambient light conditions. Full details of this study protocol are presented Villaroel *et al* [?].

4.2.1 Participant selection and Assessment

Participants needed to satisfy all of the following criteria: born at less than 37 weeks of gestation; requiring high-dependency care; requiring continuous monitoring of heart rate, respiratory rate and oxygen saturation; and requiring to be nursed naked inside an incubator. The study excluded any infants who presented life-threatening conditions that prevented the continuous monitoring in the high-dependency area of the NICU. Consent was required to be given by the babies' parents prior to any recording. Parents whose infants fulfilled the inclusion criteria were approached by the study personnel (NICU clinicians) and given full verbal and written information about the study.

4.2.2 Study set-up

The set up of all the research equipment (video recording and data storage) was designed to minimise the inconvenience to clinical staff during the study. The designated Giraffe OmniBed Carestation incubator (General Electric, Connecticut, USA) was modified by drilling a small hole in the top panel of the canopy to

allow a video camera to be positioned inside the incubator's chamber in order to film the infants without reflection and attenuation from the perspex layer (see figure ??). The study allowed for video recording to be temporarily paused, or the video camera temporarily covered, at the discretion of clinical staff during some clinical procedures such as phototherapy (for treating jaundice—yellow appearance of the skin), intravenous (IV) cannulation or when the infants were taken out of the incubator for cuddling by their parents (kangaroo care). If the infants were to be transferred to another unit, video recording was terminated and data were recorded until that point. All the standard patient monitoring and care were continued throughout the study session.



Figure 4.1: A video camera positioned over a specifically-drilled hole in the top surface of the study incubator.

4.2.3 Instrumentation

Video footage was recorded using a digital video camera positioned over the incubator inside which study infants were nursed (see figure ??). This device was set to acquire 24-bit true colour images (Red/Green/Blue, 8-bit per colour) at a pre-set rate of 20 frames per second and at a resolution of 1628×1236 pixels. Conventional vital sign data was collected concurrently by the patient monitor as part of routine care. All conventionally-monitored signals were saved on a Philips patient monitor (Philips, Amsterdam, Netherlands) and relayed to a separate workstation.

4.2.4 Data Selection

A single recording of a premature infant was selected to develop the algorithms. A 30-minute segment was selected from over 5 hours of overall recorded data for analysis. 40 minutes of Philips reference data (5 minutes before and 5 minutes after the video timestamps) was loaded around the requested camera time range to allow adjustment for differences in the Philips and camera timestamps.

4.3 Heart rate estimation

4.3.1 Overview of the process

The extraction of the PPGi signal from the video camera data involved computing the average pixel intensity from within a region of interest (ROI), filtering the resulting signal to remove non-physiological frequencies and finally detecting peaks in the resulting waveform. Motion artefacts resulting from the moving baby and moving camera were then discarded from the data using SQIs.

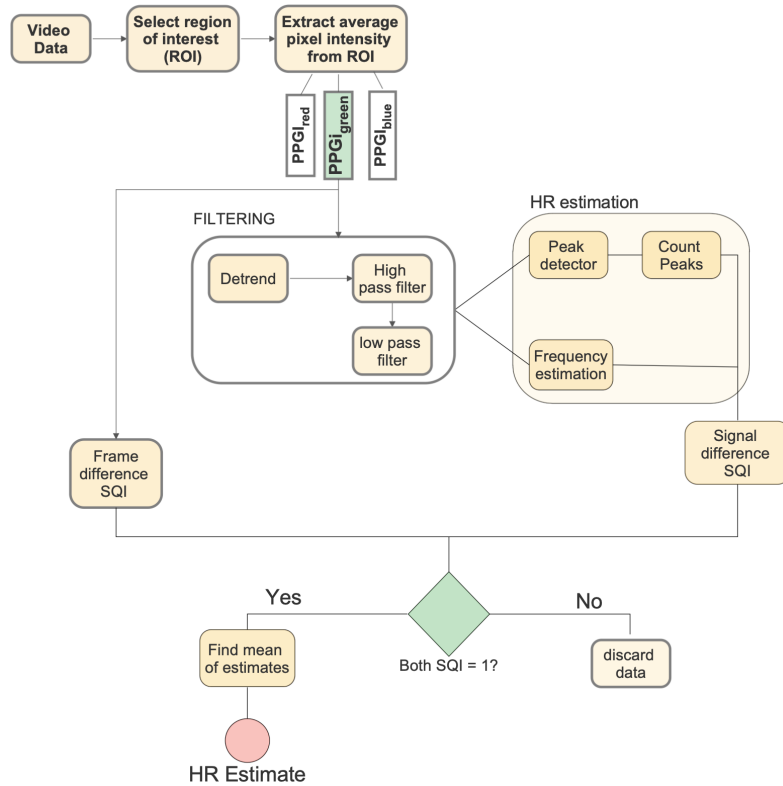


Figure 4.2: Flow diagram outlining the process of estimating HR from video data.

4.3.2 ROI Selection

One ROI was manually selected as shown in the red square in figure ?? by determining a 150×150 region on the back where skin was exposed. The mean pixel intensity within this ROI was computed for 30 minutes. Cardiac signals were extracted from the video based on the small color change on the skin that is consistent with the cardiac blood pulse. Cardiac signals were derived from the green channel as shown in figure ?? because the green channel typically contains the strongest plethysmographic signal [58].

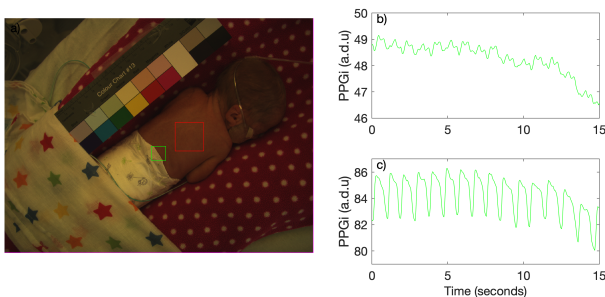


Figure 4.3: Regions of Interest and PPGi signals: a) Example video frame with ROIs for HR (in red) and RR (in green); b) Green PPGi signal extracted from the HR ROI; c) Green PPGi signal extracted from the RR ROI.

4.3.3 Filtering

The PPGi signal was first de-trended. Subsequently 70^{th} order zero-phase FIR filters with cut-off frequencies of 1.83 Hz (110 beats/min) and 2.92 Hz (175 beats/min) were designed and applied to the de-trended signal.

The magnitude response of the resulting filters is shown in figure ???. The result of applying the filters is shown in figure ??.

$$\text{icu}_H R_m \text{agresponse.png}$$

Figure 4.4: Magnitude responses. a) high-pass filter and b) low-pass filter.

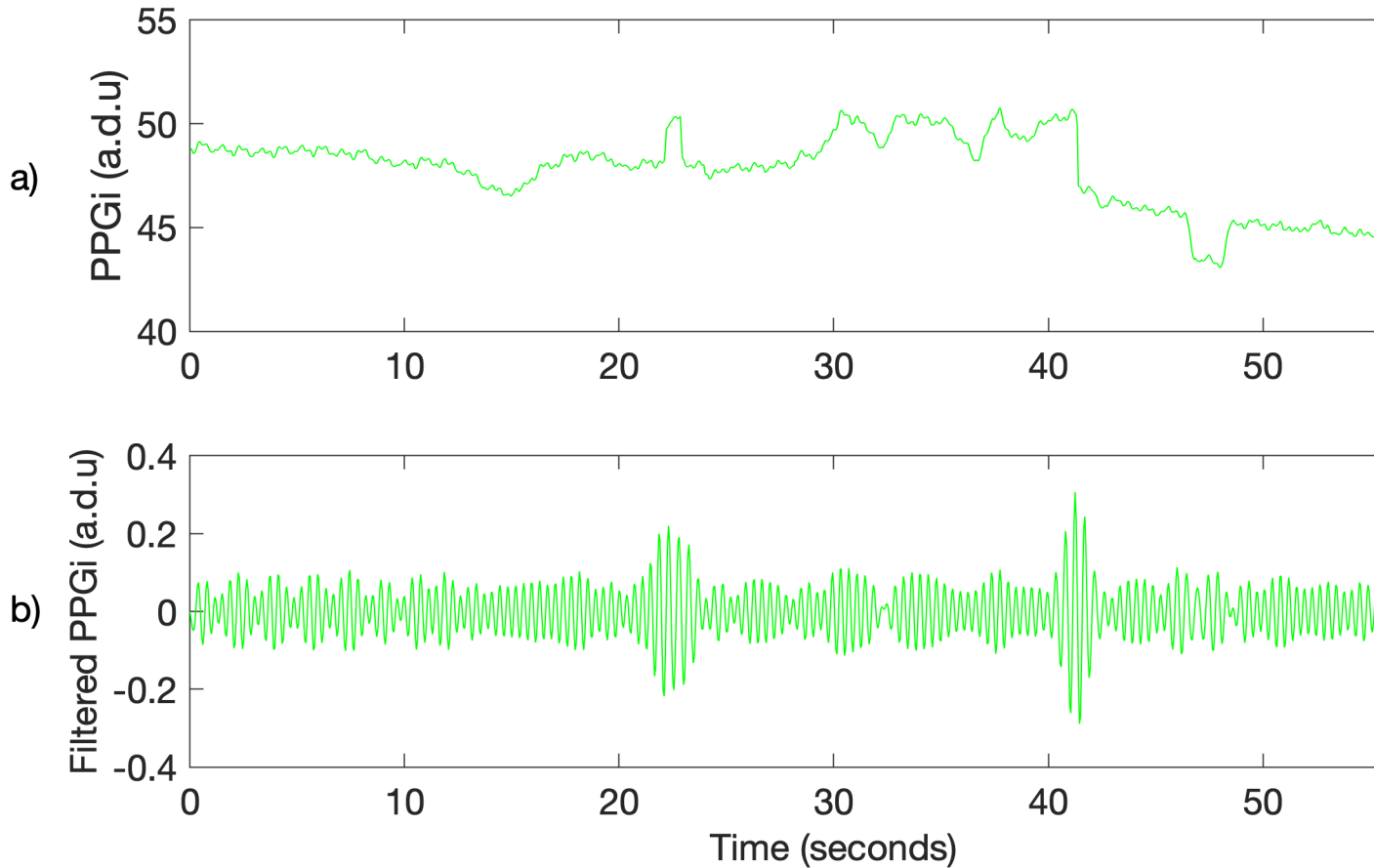


Figure 4.5: PPGi signal extracted from the HR ROI. a) Green PPGi component; b) filtered green PPGi component.

4.3.4 Peak-to-peak estimation

The filtered signal was re-sampled using a cubic spline at 75 Hz to provide better HR resolution as shown in figure ??.

Peak-to-peak analysis was then performed on the re-sampled signal. This process involved identifying prominent maximum and minimum points in the signal to represent signal amplitude. The algorithm used for peak detection first identified a peak as the i_{th} sample in a time series ts if:

$$ts(i) > ts(i-1) \text{ and } ts(i) > ts(i+1) \quad (4.1)$$

To avoid reporting erroneous peaks due to noise, identified peaks were kept where:

$$ts(i_{peak}) > \text{MinPeakHeight} \quad (4.2)$$

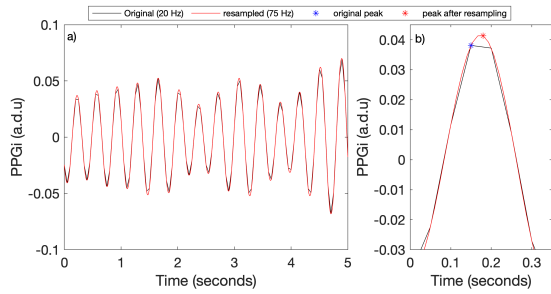


Figure 4.6: Reconstruction of a PPGi signal using cubic spline interpolation. a) The original and re-sampled signals. b) Peaks detected using the original and re-sampled waveforms.

where *MinPeakHeight* was set to a signal intensity of -0.02, based on manually observing the minimum height of waveform peaks in low intensity segments of the recording. Remaining peaks were retained if:

$$i_{peak_n} - i_{peak_{n-1}} > MinPeakDistance \quad (4.3)$$

where *MinPeakDistance* was set to give a refractory period (a recovery time after each peak) of 23 samples at 75Hz (corresponding to 200 beats/minute) based on the reference vital-sign data for the session. Finally, peaks were selected where:

$$prom(i_{peak}) > MinPeakProminence \quad (4.4)$$

where *prom* is the prominence of a peak, defined as the height of the peak relative to neighbouring troughs. Here, *MinPeakProminence* was set to a signal intensity of 0.005 based on manually observing peak prominences in several example recording segments. The algorithm then returned a vector containing the location and magnitude of each peak as shown in Fig. ??c. The FFT panels show a peak at 2.8Hz, corresponding to a HR of approximately 168 beats/minute. The reference HR recorded by the Philips monitor was 167.9 beats/minute.

icu_HR_peaks.png

Figure 4.7: 30-second analysis of filtered cardiac signals from the video camera data: a) Input signal; b) signal after filtering and c) peak detection. The FFT panels show a peak at 2.8Hz, corresponding to a HR of approximately 168 beats/minute. The reference HR recorded by the Philips monitor was 167.9 beats/minute.

4.3.5 Initial HR estimates

Two methods were used to compute HR from the video camera data. Peak-to-peak intervals, caused by...allowed the estimation of HR. The second method, Frequency estimation, used the frequency of the most prominent FFT peak to estimate HR.

Beat Counting

For this method, the time value of each peak was subtracted from the time value of the succeeding peak to get raw peak-to-peak time intervals. These were then converted into heart rates by using equation ??.

Rolling means were computed for every 20-second window, sliding by 1 second. This process was also applied to the Phillips reference signal to ensure our estimates were comparable.

$$HR = \frac{60}{peak_to_peak_interval} \quad (4.5)$$

Frequency estimation

Each 20-second window, sliding by 1 second, was de-trended and the Fast Fourier Transform (FFT) was computed. Figure ?? shows the cardiac signal and its associated frequency spectra. Each spectrum plots the magnitude of the FFT against frequency. The figure shows that the selected green channel contains a prominent low-frequency content and cardiac component (the latter at approximately 2.8 Hz, or 168 beats/minute). The low frequency is filtered out as shown in the FFT plot of figure ??b. The frequency of the remaining FFT peak was taken as an estimate for the HR frequency in that window.

4.3.6 Signal Quality assessment

Two signal quality index algorithms are proposed: signal difference and frame difference. Figure ?? shows a 120-second sample plot of the two proposed methods.

Signal Difference SQI

The agreement between the two estimation methods (peak-to-peak and FFT) was used to create an HR difference SQI. This SQI was set to 1 if the two estimates were within 3 beats/min, and set to 0 otherwise.

Frame Difference SQI

A frame difference signal was created by comparing the intensity of the pixels between two subsequent frames. This was done by taking the mean of the absolute differences between each pair of pixels.

$$diff_{frame} = \frac{\sum_x \sum_y \text{abs}(frame(x, y, i) - frame(x, y, i - 1))}{\text{len}(x) \times \text{len}(y)} \quad (4.6)$$

where $frame(x, y, i)$ is a pixel with coordinates x and y in the i^{th} frame, $\text{len}(x)$ is the width of the frame and $\text{len}(y)$ is the height of the frame. Changes in lighting or movement should cause bigger changes in intensity, indicating regions of poor signal quality. If this difference in pixel intensity was greater than a threshold value of mean + 1.6 × standard deviation, the SQI was set to 0.

4.3.7 Estimating HR

Following the signal quality assessment, HR was estimated using a 20-second sliding window with a step size of 1 second. If either the signal or frame difference SQIs were 0, the window was taken as a poor-quality window and was discarded. If both SQIs were equal to 1, HR for that window was estimated as:

$$HR_{estimate} = \frac{HR_{FFT} + HR_{peak-to-peak}}{2} \quad (4.7)$$

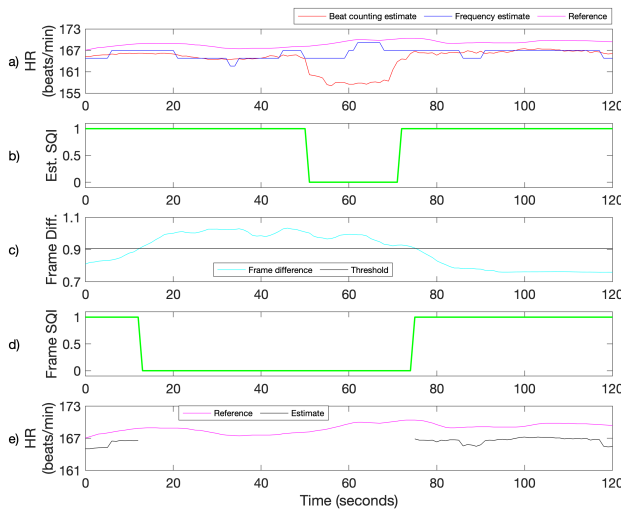


Figure 4.8: Using SQI to discard noisy data. Periods of high movement were removed using signal quality indices. a) Beat counting and frequency estimates in comparison to the reference HR estimate; b) Signal difference SQI; c) Frame difference; d) Frame difference SQI; e) Comparison between reference and HR estimate.

icu_Output_R.png

Figure 4.9: Flow diagram outlining the process of estimating RR from video data.

4.4 Respiratory rate estimation

4.4.1 Overview of the process

Figure ?? presents an overview of the methods used to estimate RR from video camera data. The raw PPGi signal was extracted by taking the mean of the pixel intensity from a ROI over the patient's back. Two digital filters were used to suppress frequency components below 0.25 Hz and above 1.42 Hz, corresponding to a respiratory rate range approximately between 15 to 85 breaths/min. A peak detection method was applied to filtered the signal to identify prominent points. Subsequently, the quality of the PPGi signal was analysed to identify areas of good-quality respiratory signal. RR estimates were computed for periods for which the PPGi signal was judged to be of good quality.

4.4.2 ROI Selection

Breathing causes volume changes of the infant's lungs which in turn causes movement of the body. This movement can be captured by a video camera from areas containing exposed skin or covered by tight-fitting clothing such as a nappy. Respiratory signals can therefore be extracted from the respiration induced chest/abdomen motion. One ROI of size 75 x 75 pixels, was manually selected and the mean pixel intensity within the selected ROI was computed for each video frame (see figure ??). As with HR, only the green channel was used for processing.

4.4.3 Filtering

The respiratory signal extracted from the selected ROI was de-trended by fitting a straight line to the data using linear regression and subtracting this straight line from the data. The de-trended data was further

processed by applying two IIR filters to remove low and high frequency noise from the signal. A 2nd order high-pass and low-pass filter were designed with cut-off frequencies of 0.25 Hz (15 breaths/min) and 1.42 Hz (85 breaths/min), respectively (see figure ??). The result of applying the filters to a sample time series extracted from the video camera data is shown in figure ??.

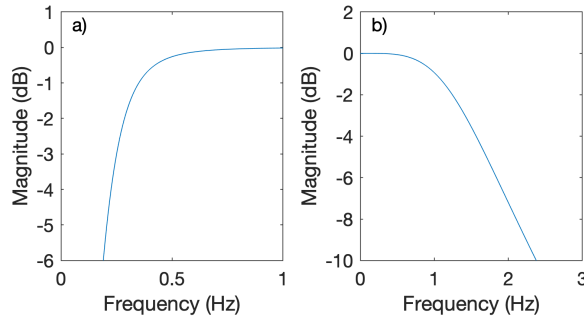


Figure 4.10: Magnitude responses for extracting a respiratory signal from the video camera data. a) High-pass filter and b) low-pass filter.

4.4.4 Peak-to-peak estimation

The filtered signal was re-sampled using a cubic spline at 75 Hz to provide better RR resolution. Local peaks found were then found by using the the algorithms described in section ???. This analysis was done using MinPeakDistance of 12.0 ms (83.3 breaths/min), MinPeakHeight of -15.0 and MinPeakProminence of 0.05. The algorithm then returned a vector containing the result of the location and magnitude of each peak as shown in figure Fig. ??.

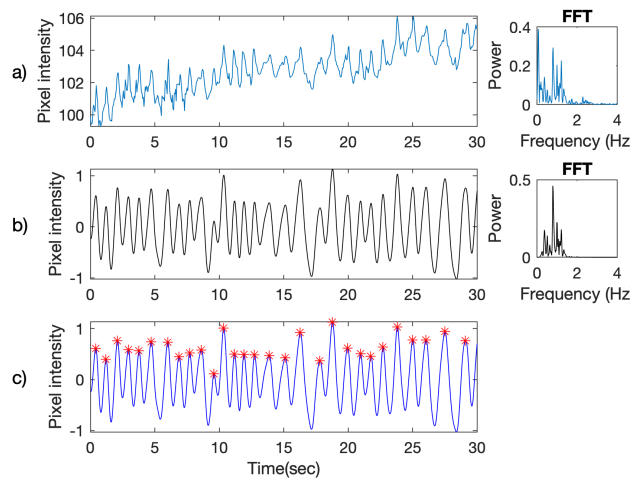


Figure 4.11: Peak detection for a 30-second sample respiratory signal. a) Input signal; b) Signal after filtering and c) detected peaks.

The time value of each peak was subtracted from the time value of the succeeding peak to get raw breath length estimates. These were then converted into respiratory rates by using equation ???. Rolling medians were computed over a 40-second window sliding by 5 second. This process was also applied to the Phillips reference signal to ensure our estimates were comparable.

$$RR = \frac{60}{breath_length} \quad (4.8)$$

4.4.5 Respiratory signal quality assessment

Frame Difference SQI

Changes in lighting or movement caused large changes in light intensity recorded by the video camera. The pixel intensity of every frame was averaged and subtracted to that of the succeeding frame. If the difference in pixel intensity was greater than a threshold value, the SQI was set to 0 as demonstrated in figure ??.

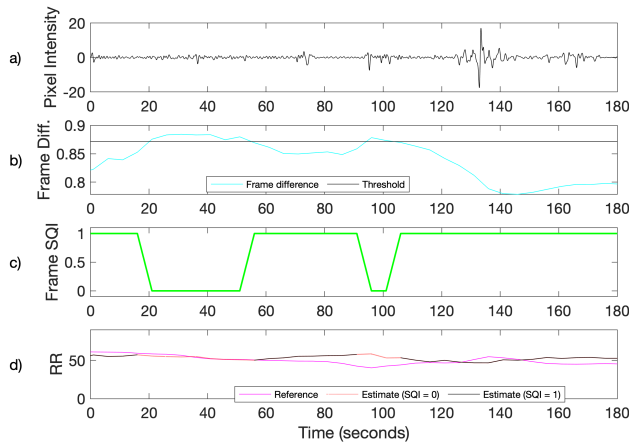


Figure 4.12: Using SQI to discard noisy data. Periods of high movement are removed using signal quality index. a) Filtered PPGI signal; b) Frame difference; c) Frame difference SQI; d) Comparison between reference and HR estimate.

4.4.6 Estimating RR

If the frame difference SQI was set to 1, the peak-to-peak estimate was taken as the final RR estimate for each 40-second window, sliding by 5 seconds. The estimated RR was then compared to the reference values provided by the Philips monitor.

4.5 Results

4.5.1 Heart rate

Figure ?? shows a comparison between the estimated HR and the reference values reported by the Philips monitor. Figure ?? shows a set of summary performance plots for the proposed HR estimation algorithms.

4.5.2 Respiratory rate

Figure ?? shows a comparison between the estimated RR and the reference values provided by the Philips monitor. Figure ?? shows a set of summary performance plots for the proposed RR estimation algorithms.

4.5.3 Summary metrics

Table ?? shows overall performance metrics for estimating heart rate and respiratory rate from the video camera for the selected recording session.

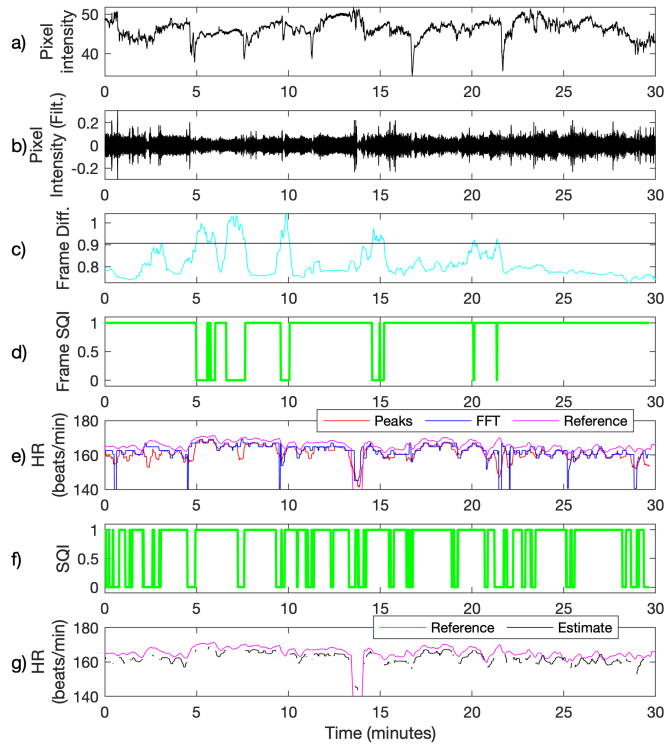


Figure 4.13: Heart rate estimation for a 30-minute recording session. a) Pixel intensity signal; b) Filtered pixel intensity signal; c) Frame difference and d) Frame difference SQL; e) Comparison between reference and peak and FFT estimates; f) Signal difference SQL; g) Comparison between reference and HR estimate.

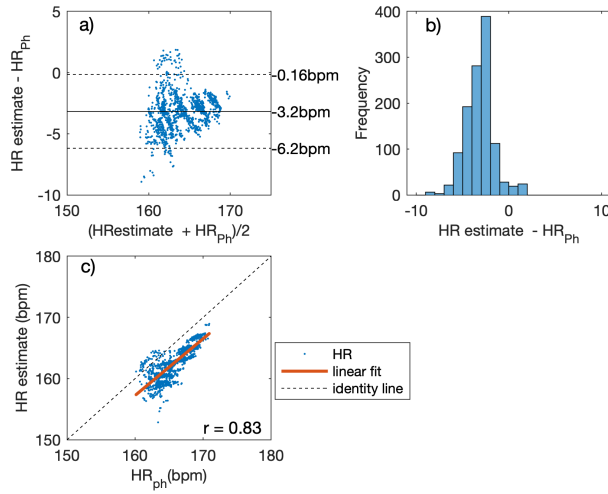


Figure 4.14: Comparison between the reference and estimated heart rate estimates. a) Bland-Altman plot; b) Histogram of the differences between the two HR estimates and c) Correlation plot shows a positive correlation between the two measurements. The red line represents the linear fit.

4.6 Discussion

Heart rate can be estimated from the video camera data because changes in blood volume due to the cardiac cycle lead to subtle color changes in skin recorded by the video camera. As can be seen in figure ?? and table ??, the estimated heart rate was comparable to the values provided by the reference medical

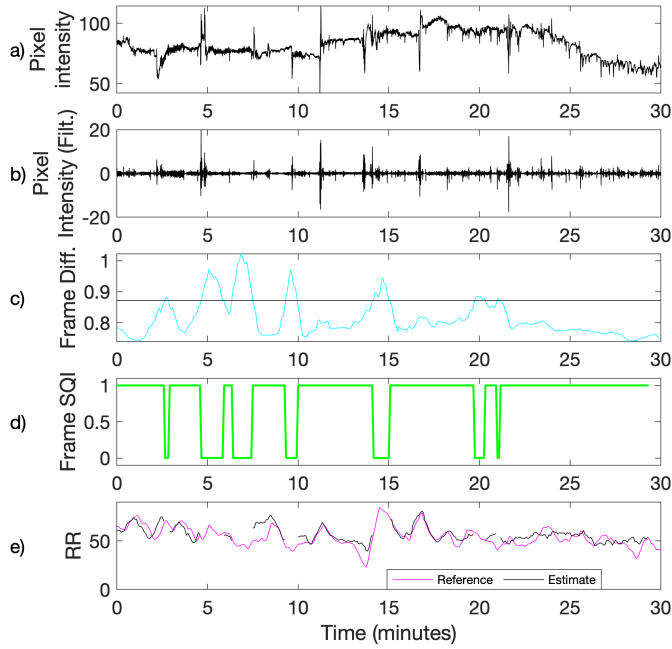


Figure 4.15: Respiratory rate estimation for a 30-minute recording session. a) Pixel intensity signal; b) Filtered pixel intensity signal; c) Frame difference and d) Frame difference SQI e) Comparison between reference and RR estimate.

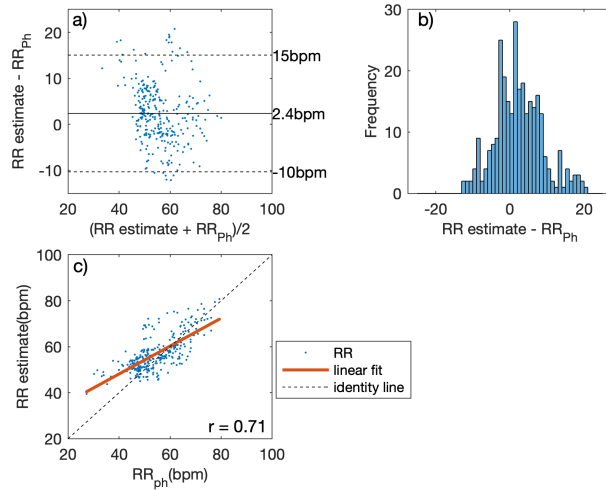


Figure 4.16: Comparison between the reference and estimated respiratory rate a) Bland-Altman plot. b) Histogram of the differences between the two RR estimates and c) Correlation plot shows a positive correlation between the two measurements. The red line represents the linear fit.

device. The mean bias of 3.2 beats/min and correlation coefficient of 0.83 suggest that our signal processing methods performed adequately. Most of the errors were the result of motion artefacts, caused by the camera moving or clinical interventions by the nurses. The Frame difference SQI was successful in removing most of these periods. The two proposed methods, FFT and beat counting, performed adequately for the whole session selected and, therefore, the SQI did not discard a substantial proportion of the HR estimated data.

To extract a respiratory signal from video camera data, the movement of the nappy and exposed skin

Table 4.1: Summary of error analysis for the proposed algorithms for RR and HR computation from video camera data.

	MAE*	MAD*	RMSE*	r
HR	3.2	1.1	3.5	0.83
RR	5.3	5.0	6.9	0.71

* Values in beats/min for HR or breaths/min for RR

was used. Comparisons between RR provided by the Philips monitor and the estimated RR showed varied performance. The correlation coefficient ($r = 0.71$) and relatively greater errors (MAE of 5.3 and MAD of 5.0) in figure ?? and table ?? respectively, are clear indication of this. Overall, we were able extract and estimate RR using SQIs to isolate time periods with good quality data. It is worth noting when interpreting the results obtained that the estimates provided by the Philips monitor are noisy, clinical staff often compute RR manually.

4.7 Conclusion

In this chapter, video data from a study on premature infants was analysed, employing signal processing methods to extract cardiac and respiratory signals and estimate RR and HR. The study comprised recording video data under a real hospital scenario, regular patient care was not disrupted. The pre-term infants monitored were active and clinical staff routinely interacted with them. This dataset presents a recording scenario that will be comparable to the recordings of children diagnosed with pneumonia in our future clinical study in Kenya. Therefore, the algorithms proposed in this chapter will be expanded and improved during the next phase of my DPhil.

The HR results in this chapter had a positive correlation of 0.83. An RMSE of 3.5 beats/min was achieved using the video camera for HR estimation. RR estimation was also successful, with a correlation coefficient of $R= 0.71$. An RMSE of 6.9 was achieved from the non-contact RR estimation. The methods developed in this chapter will form the foundation for algorithms to estimate vital signs from video camera data from children diagnosed with pneumonia, which will be developed during the second year of my DPhil.

Bibliography

- [1] Paul S Addison, James N Watson, Michael L Mestek, and Roger S Mecca. Developing an algorithm for pulse oximetry derived respiratory rate (rr oxi): A healthy volunteer study. *Journal of clinical monitoring and computing*, 26(1):45–51, 2012.
- [2] Asad Ali, Asif Raza Khowaja, Maaman Zahoor Bashir, Fatima Aziz, Sultan Mustafa, and Anita Zaidi. Role of human metapneumovirus, influenza a virus and respiratory syncytial virus in causing who-defined severe pneumonia in children in a developing country. *PloS one*, 8(9):e74756, 2013.
- [3] Philip Ayieko and Mike English. Case management of childhood pneumonia in developing countries. *The Pediatric infectious disease journal*, 26(5):432, 2007.
- [4] Ying-Wen Bai, Wen-Tai Li, and Cheng-Hsiang Yeh. Design and implementation of an embedded monitor system for body breath detection by using image processing methods. In *2010 Digest of Technical Papers International Conference on Consumer Electronics (ICCE)*, pages 193–194. IEEE, 2010.
- [5] Raquel Bailón, Leif Sornmo, and Pablo Laguna. A robust method for ecg-based estimation of the respiratory frequency during stress testing. *IEEE transactions on biomedical engineering*, 53(7):1273–1285, 2006.
- [6] Andrew Bastawrous and Matthew J Armstrong. Mobile health use in low-and high-income countries: an overview of the peer-reviewed literature. *Journal of the royal society of medicine*, 106(4):130–142, 2013.
- [7] Robert E Black, Simon Cousens, Hope L Johnson, Joy E Lawn, Igor Rudan, Diego G Bassani, Prabhat Jha, Harry Campbell, Christa Fischer Walker, Richard Cibulskis, et al. Global, regional, and national causes of child mortality in 2008: a systematic analysis. *The lancet*, 375(9730):1969–1987, 2010.
- [8] Paolo Bonato. Advances in wearable technology and applications in physical medicine and rehabilitation, 2005.
- [9] Martine JM Breteler, Erik Huizinga, Kim van Loon, Luke PH Leenen, Daan AJ Dohmen, Cor J Kalkman, and Taco J Blokhuis. Reliability of wireless monitoring using a wearable patch sensor in high-risk surgical patients at a step-down unit in the netherlands: a clinical validation study. *BMJ open*, 8(2):e020162, 2018.
- [10] Denisse Castaneda, Aibhlin Esparza, Mohammad Ghamari, Cinna Soltanpur, and Homer Nazeran. A review on wearable photoplethysmography sensors and their potential future applications in health care. *International journal of biosensors & bioelectronics*, 4(4):195, 2018.
- [11] Sitthichok Chaichulee. Non-contact vital sign monitoring of pre-term infants. PhD thesis, University of Oxford, 2018.
- [12] Thomas Cherian, E Kim Mulholland, John B Carlin, Harald Ostensen, Ruhul Amin, Margaret de Campo, David Greenberg, Rosanna Lagos, Marilla Lucero, Shabir A Madhi, et al. Standardized interpretation of paediatric chest radiographs for the diagnosis of pneumonia in epidemiological studies. *Bulletin of the World Health Organization*, 83:353–359, 2005.
- [13] Trevor Duke, Rami Subhi, David Peel, and Bernhard Frey. Pulse oximetry: technology to reduce child mortality in developing countries. *Annals of tropical paediatrics*, 29(3):165–175, 2009.
- [14] Mohamed Elgendi, Richard Fletcher, Yongbo Liang, Newton Howard, Nigel H Lovell, Derek Abbott, Kenneth Lim, and Rabab Ward. The use of photoplethysmography for assessing hypertension. *NPJ digital medicine*, 2(1):1–11, 2019.
- [15] Susannah G Fleming and Lionel Tarassenko. A comparison of signal processing techniques for the extraction of breathing rate from the photoplethysmogram. *Int. J. Biol. Med. Sci.*, 2(4):232–236, 2007.
- [16] AM Gadomski, Nagwa Khallaf, Samy El Ansary, and Robert E Black. Assessment of respiratory rate and chest indrawing in children with ari by primary care physicians in egypt. *Bulletin of the World Health Organization*, 71(5):523, 1993.
- [17] Amy Sarah Ginsburg, Salim Sadruddin, and Keith P Klugman. Innovations in pneumonia diagnosis and treatment: a call to action on world pneumonia day, 2013. *The Lancet Global Health*, 1(6):e326–e327, 2013.

- [18] Amy Sarah Ginsburg, Jaclyn Delarosa, Waylon Brunette, Shahar Levari, Mitch Sundt, Clarice Larson, Charlotte Tawiah Agyemang, Sam Newton, Gaetano Borriello, and Richard Anderson. mpneumonia: development of an innovative mhealth application for diagnosing and treating childhood pneumonia and other childhood illnesses in low-resource settings. *PloS one*, 10(10):e0139625, 2015.
- [19] Amy Sarah Ginsburg, Jennifer L Lenahan, Rasa Izadnegahdar, and J Mark Ansermino. A systematic review of tools to measure respiratory rate in order to identify childhood pneumonia. *American journal of respiratory and critical care medicine*, 197(9):1116–1127, 2018.
- [20] Dina Goodman, Mary E Crocker, Farhan Pervaiz, Eric D McCollum, Kyle Steenland, Suzanne M Simkovich, Catherine H Miele, Laura L Hammitt, Phabiola Herrera, Heather J Zar, et al. Challenges in the diagnosis of paediatric pneumonia in intervention field trials: recommendations from a pneumonia field trial working group. *The Lancet Respiratory Medicine*, 7(12):1068–1083, 2019.
- [21] Stephen M Graham, Mike English, Tabish Hazir, Penny Enarson, and Trevor Duke. Challenges to improving case management of childhood pneumonia at health facilities in resource-limited settings. *Bulletin of the World Health Organization*, 86:349–355, 2008.
- [22] Gavin B Grant, Harry Campbell, Scott F Dowell, Stephen M Graham, Keith P Klugman, E Kim Mulholland, Mark Steinhoff, Martin W Weber, and Shamim Qazi. Recommendations for treatment of childhood non-severe pneumonia. *The Lancet Infectious Diseases*, 9(3):185 – 196, 2009. ISSN 1473-3099. doi: [https://doi.org/10.1016/S1473-3099\(09\)70044-1](https://doi.org/10.1016/S1473-3099(09)70044-1). URL <http://www.sciencedirect.com/science/article/pii/S1473309909700441>.
- [23] Tao Guo, Zhengtao Cao, Zhengbo Zhang, Deyu Li, and Mengsun Yu. Reflective oxygen saturation monitoring at hypothenar and its validation by human hypoxia experiment. *Biomedical engineering online*, 14(1):76, 2015.
- [24] Vandana Gupta and Mark Woodhead. Oxygen saturation and pneumonia: a complement to current practice or another burden for the gp? *Primary care respiratory journal: journal of the General Practice Airways Group*, 19(4):301, 2010.
- [25] Vishal Gupta and Vinod Kumar Sharma. Skin typing: Fitzpatrick grading and others. *Clinics in Dermatology*, 37(5):430–436, 2019.
- [26] Sangjin Hong, Jinseok Lee, Akshay Athalye, Petar M Djuric, and We-Duke Cho. Design methodology for domain specific parameterizable particle filter realizations. *IEEE Transactions on Circuits and Systems I: Regular Papers*, 54(9):1987–2000, 2007.
- [27] Joao Jorge, Mauricio Villarroel, Sitthichok Chaichulee, Alessandro Guazzi, Sara Davis, Gabrielle Green, Kenny McCormick, and Lionel Tarassenko. Non-contact monitoring of respiration in the neonatal intensive care unit. In *2017 12th IEEE International Conference on Automatic Face & Gesture Recognition (FG 2017)*, pages 286–293. IEEE, 2017.
- [28] Walter Karlen, Heng Gan, Michelle Chiu, Dustin Dunsmuir, Guohai Zhou, Guy A Dumont, and J Mark Ansermino. Improving the accuracy and efficiency of respiratory rate measurements in children using mobile devices. *PloS one*, 9(6):e99266, 2014.
- [29] Jinseok Lee and Ki H Chon. Respiratory rate extraction via an autoregressive model using the optimal parameter search criterion. *Annals of biomedical engineering*, 38(10):3218–3225, 2010.
- [30] Chia-Hung Lien, Po-Tsun Chen, Ying-Wen Bai, and Ming-Bo Lin. Monitoring system with moving object detection based on msn messenger. In *2008 IEEE Instrumentation and Measurement Technology Conference*, pages 229–234. IEEE, 2008.
- [31] Sumit R Majumdar, Dean T Eurich, John-Michael Gamble, A Senthilselvan, and Thomas J Marrie. Oxygen saturations less than 92% are associated with major adverse events in outpatients with pneumonia: a population-based cohort study. *Clinical infectious diseases*, 52(3):325–331, 2011.
- [32] David A McAllister, Li Liu, Ting Shi, Yue Chu, Craig Reed, John Burrows, Davies Adeloye, Igor Rudan, Robert E Black, Harry Campbell, et al. Global, regional, and national estimates of pneumonia morbidity and mortality in children younger than 5 years between 2000 and 2015: a systematic analysis. *The Lancet Global Health*, 7(1):e47–e57, 2019.
- [33] Eric D McCollum and Amy Sarah Ginsburg. Outpatient management of children with world health organization chest indrawing pneumonia: implementation risks and proposed solutions. *Clinical Infectious Diseases*, 65(9):1560–1564, 2017.
- [34] George H Mccracken Jr et al. Diagnosis and management of pneumonia in children. *The Pediatric infectious disease journal*, 19(9):924–928, 2000.

- [35] Yitzhak Mendelson. Pulse oximetry: theory and applications for noninvasive monitoring. *Clinical chemistry*, 38(9):1601–1607, 1992.
- [36] David R Murdoch, Katherine L O'Brien, J Anthony G Scott, Ruth A Karron, Niranjan Bhat, Amanda J Driscoll, Maria Deloria Knoll, and Orin S Levine. Breathing new life into pneumonia diagnostics. *Journal of clinical microbiology*, 47(11):3405–3408, 2009.
- [37] K Nakajima, T Tamura, and H Miike. Monitoring of heart and respiratory rates by photoplethysmography using a digital filtering technique. *Medical engineering & physics*, 18(5):365–372, 1996.
- [38] Elina Naydenova. *Machine learning for childhood pneumonia diagnosis*. PhD thesis, University of Oxford, 2018.
- [39] Lena Nilsson, Anders Johansson, and Sigga Kalman. Monitoring of respiratory rate in postoperative care using a new photoplethysmographic technique. *Journal of clinical monitoring and computing*, 16(4):309–315, 2000.
- [40] Aaltje Camielle Noordam, Yolanda Barberá Laínez, Salim Sadruddin, Pabla María van Heck, Alex Opio Chono, Geoffrey Larry Acaye, Victor Lara, Agnes Nanyonjo, Charles Ocan, and Karin Källander. The use of counting beads to improve the classification of fast breathing in low-resource settings: a multi-country review. *Health Policy and Planning*, 30(6):696–704, 2015.
- [41] World Health Organization. *Pocket book of hospital care for children: guidelines for the management of common childhood illnesses*. World Health Organization, 2013.
- [42] World Health Organization et al. Integrated management of childhood illness: caring for newborns and children in the community, 2011.
- [43] Farhan Pervaiz, Miguel A Chavez, Laura E Ellington, Matthew Grigsby, Robert H Gilman, Catherine H Miele, Dante Figueroa-Quintanilla, Patricia Compen-Chang, Julio Marin-Concha, Eric D McCollum, et al. Building a prediction model for radiographically confirmed pneumonia in peruvian children: from symptoms to imaging. *Chest*, 154(6):1385–1394, 2018.
- [44] Igor Rudan, Katherine L O'brien, Harish Nair, Li Liu, Evropi Theodoratou, Shamim Qazi, Ivana Lukšić, Christa L Fischer Walker, Robert E Black, Harry Campbell, et al. Epidemiology and etiology of childhood pneumonia in 2010: estimates of incidence, severe morbidity, mortality, underlying risk factors and causative pathogens for 192 countries. *Journal of global health*, 3(1), 2013.
- [45] Fiona M Russell, Rita Reyburn, Jocelyn Chan, Evelyn Tuivaga, Ruth Lim, Jana Lai, Hoang Minh Tu Van, Molina Choummavong, Vanphanom Sychareun, Dung Khu Thi Khanh, et al. Impact of the change in who's severe pneumonia case definition on hospitalized pneumonia epidemiology: case studies from six countries. *Bulletin of the World Health Organization*, 97(6):386, 2019.
- [46] Malay Sarkar, Irappa Madabhavi, Narasimhalu Niranjan, and Megha Dogra. Auscultation of the respiratory system. *Annals of thoracic medicine*, 10(3):158, 2015.
- [47] Sonal N Shah, Richard G Bachur, David L Simel, and Mark I Neuman. Does this child have pneumonia?: the rational clinical examination systematic review. *Jama*, 318(5):462–471, 2017.
- [48] Sergio Stagno, Dana M Brasfield, Mary B Brown, Gail H Cassell, Linda L Pifer, Richard J Whitley, and Ralph E Tiller. Infant pneumonitis associated with cytomegalovirus, chlamydia, pneumocystis, and ureaplasma: a prospective study. *Pediatrics*, 68(3):322–329, 1981.
- [49] Rami Subhi, Matthew Adamson, Harry Campbell, Martin Weber, Katherine Smith, Trevor Duke, Hypoxaemia in Developing Countries Study Group, et al. The prevalence of hypoxaemia among ill children in developing countries: a systematic review. *The Lancet infectious diseases*, 9(4):219–227, 2009.
- [50] Yu Sun and Nitish Thakor. Photoplethysmography revisited: from contact to noncontact, from point to imaging. *IEEE Transactions on Biomedical Engineering*, 63(3):463–477, 2015.
- [51] Reijo Takalo, Heli Hytti, and Heimo Ihälainen. Tutorial on univariate autoregressive spectral analysis. *Journal of clinical monitoring and computing*, 19(6):401–410, 2005.
- [52] K Song Tan, Reza Saatchi, Heather Elphick, and Derek Burke. Real-time vision based respiration monitoring system. In *2010 7th International Symposium on Communication Systems, Networks & Digital Signal Processing (CSNDSP 2010)*, pages 770–774. IEEE, 2010.
- [53] L Tarassenko, M Villarroel, A Guazzi, J Jorge, DA Clifton, and C Pugh. Non-contact video-based vital sign monitoring using ambient light and auto-regressive models. *Physiological measurement*, 35(5):807, 2014.

- [54] London: Save the Children. Save the children. fighting for breath: a call to action on childhood pneumonia. <https://www.savethechildren.org.uk/content/dam/global/reports/health-and-nutrition/fighting-for-breath-low-res.pdf>, Accessed: 2020-10-31.
- [55] Christopher Troeger, Mohammad Forouzanfar, Puja C Rao, Ibrahim Khalil, Alexandria Brown, Scott Swartz, Nancy Fullman, Jonathan Mosser, Robert L Thompson, Robert C Reiner Jr, et al. Estimates of the global, regional, and national morbidity, mortality, and aetiologies of lower respiratory tract infections in 195 countries: a systematic analysis for the global burden of disease study 2015. *The Lancet Infectious Diseases*, 17(11):1133–1161, 2017.
- [56] Christopher Troeger, Brigette Blacker, Ibrahim A Khalil, Puja C Rao, Jackie Cao, Stephanie RM Zimsen, Samuel B Albertson, Aniruddha Deshpande, Tamer Farag, Zegeye Abebe, et al. Estimates of the global, regional, and national morbidity, mortality, and aetiologies of lower respiratory infections in 195 countries, 1990–2016: a systematic analysis for the global burden of disease study 2016. *The Lancet infectious diseases*, 18(11):1191–1210, 2018.
- [57] Håkan Ugnell and PÅ Öberg. The time-variable photoplethysmographic signal; dependence of the heart synchronous signal on wavelength and sample volume. *Medical engineering & physics*, 17(8):571–578, 1995.
- [58] Wim Verkruyse, Lars O Svaasand, and J Stuart Nelson. Remote plethysmographic imaging using ambient light. *Optics express*, 16(26):21434–21445, 2008.
- [59] Mauricio Villarroel, Alessandro Guazzi, João Jorge, Sara Davis, Peter Watkinson, Gabrielle Green, Asha Shenvi, Kenny McCormick, and Lionel Tarassenko. Continuous non-contact vital sign monitoring in neonatal intensive care unit. *Healthcare technology letters*, 1(3):87–91, 2014.
- [60] Mauricio Villarroel, João Jorge, Chris Pugh, and Lionel Tarassenko. Non-contact vital sign monitoring in the clinic. In *2017 12th IEEE International Conference on Automatic Face & Gesture Recognition (FG 2017)*, pages 278–285. IEEE, 2017.
- [61] Tessa M Wardlaw, Emily White Johansson, and Matthew J Hodge. *Pneumonia: the forgotten killer of children*. Unicef, 2006.
- [62] HJ Zar, SA Madhi, SJ Aston, and SB Gordon. Pneumonia in low and middle income countries: progress and challenges. *Thorax*, 68(11):1052–1056, 2013.